

# CHIMERA: Adaptive Cache Injection and Semantic Anchor Prompting for Zero-shot Image Morphing with Morphing-oriented Metrics

Dahyeon Kye<sup>1\*</sup> Jeahun Sung<sup>1\*</sup> MinKyu Jeon<sup>2</sup> Jihyong Oh<sup>1†</sup>

<sup>1</sup> Chung-Ang University <sup>2</sup> Princeton University

{rpekgus, jhseong, jihyongoh}@cau.ac.kr mj7341@princeton.edu

<https://cmlab-korea.github.io/CHIMERA/>



Figure 1. **Key challenges in morphing and a user study with our morphing-oriented metric (GLCS).** Existing methods struggle with smoothness, domain consistency, and perceptual quality (red arrows), while our approach (CHIMERA) produces coherent transitions across all three. Standard metrics (FID, LPIPS [57], PPL [22]) fail to reflect true morphing quality, whereas user study results on two datasets [7, 27] align closely with our proposed GLCS ranking, validating GLCS as a morphing-oriented metric.

## Abstract

Diffusion models exhibit remarkable generative ability, yet achieving smooth and semantically consistent image morphing remains a challenge. Existing approaches often yield abrupt transitions or over-saturated appearances due to the lack of adaptive structural and semantic alignments. We propose CHIMERA, a zero-shot diffusion-based framework that formulates morphing as a cached inversion-guided de-

noising process. To handle large semantic and appearance disparities, we propose Adaptive Cache Injection and Semantic Anchor Prompting. Adaptive Cache Injection (ACI) caches down, mid, and up blocks’ features from both inputs during DDIM inversion and re-injects them adaptively during denoising in depth- and timestep-adaptive manners, enabling natural feature fusion and smooth transitions. Semantic Anchor Prompting (SAP) leverages a vision-language model to generate a shared anchor-prompt that serves as a semantic anchor, bridging dissimilar inputs and guiding the denoising process toward coherent re-

\*Co-first authors (equal contribution).

†Corresponding author.

sults. Finally, we introduce the *Global-Local Consistency Score (GLCS)*, a morphing-oriented metric that simultaneously evaluates the global harmonization of the two inputs and the smoothness of the local morphing transition. Extensive experiments and user studies show that CHIMERA achieves smoother and more semantically aligned transitions than existing methods, establishing a new state-of-the-art in image morphing. The code and project page will be publicly released.

## 1. Introduction

Image morphing aims to generate perceptually smooth and visually coherent transitions between two given images. Classical morphing techniques rely on handcrafted geometric correspondences or optical-flow-based warping [4], which often fail when structural layouts or semantic content differ substantially. Recently, diffusion-based morphing frameworks [7, 24, 27, 47, 49] have achieved notable progress by interpolating in the latent space of pre-trained diffusion models [39, 43], producing high-fidelity intermediate images without explicit correspondence estimation. Nevertheless, these methods still suffer from instability in structure and discontinuity in semantics, especially when handling cross-domain, i.e. heterogeneous, or weakly correlated inputs. Existing tuning-based diffusion methods [24, 27] enhance perceptual smoothness by fine-tuning diffusion models [39] with morphing-specific objectives, enabling smoother transitions. However, these approaches are sample-specific and require retraining or adaptation for different image pairs or domains, making them computationally expensive and poorly generalizable to novel domains. In contrast, FreeMorph [7] adopts a training-free strategy by performing DDIM inversion [32] on interpolated latent representations of the two given inputs, which initializes the reverse diffusion process with interpolated latent states. This approach effectively enhances image fidelity and eliminates blurriness. However, since the denoising process operates without any additional guidance, it often produces over-saturated, synthetic-looking images and fails to blend domain-specific characteristics (e.g., photographs vs. illustrations) [14, 20]. Consequently, FreeMorph preserves local appearance details well but fails to maintain global domain coherence. Tuning-based methods [24, 27] offer stronger alignment but incur extra training and computational cost. As shown in Fig. 1, these trade-offs manifest as complementary strengths and weaknesses across smoothness, domain consistency, and perceptual quality, and motivate the need for a morphing method that can jointly achieve all three. As shown in Fig. 2, existing methods typically excel in either structural fidelity, visual realism, or semantic coherence, but fail to achieve all three simultaneously.

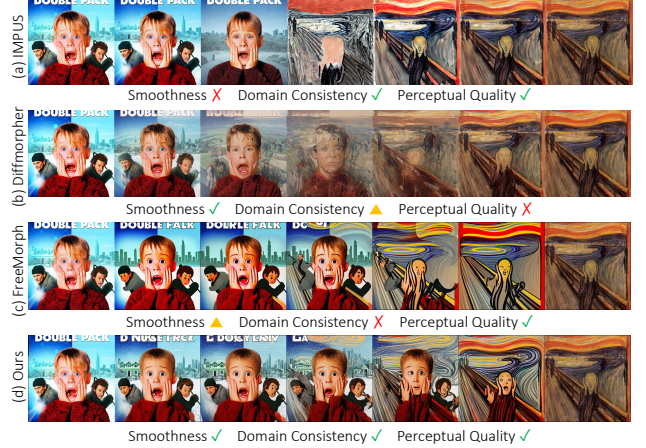


Figure 2. **Qualitative result of smoothness of morphing transition (Smooth), heterogeneous-aware domain consistency (Domain Consistency), and perceptual quality (Perceptual Quality).** Here, **X** indicates cases that fail for most pairs, **▲** represents cases that fail for some pairs, and **✓** denotes cases that succeed for most pairs.

To overcome these limitations, we propose CHIMERA (Adaptive Cache Injection and Semantic Anchor Prompting for ZERO-shot Image Morphing with Morphing-oriented Metrics), a zero-shot diffusion-based image morphing framework. CHIMERA introduces two complementary modules, Adaptive Cache Injection (ACI) and Semantic Anchor Prompting (SAP) to effectively guide the denoising process toward spatially semantic consistencies. ACI mitigates instability and over-saturation by reusing cached multi-stage and -timestep DDIM inversion features of both inputs and adaptively re-injecting them into the denoising U-Net [40] in a depth layer- and denoising timestep-adaptive manners. Since early down-block features of U-Net preserve globally coarse spatial structure, while deeper up-block features refine appearance and domain-specific details, our hierarchical cache guides spatially stable and visually consistent morphs that maintain fidelity while seamlessly bridging domain differences of the given two inputs. While ACI ensures visual and structural consistency, morphing remains challenging when the two inputs share little semantic or layout correspondence. To address this, Semantic Anchor Prompting (SAP) introduces high-level semantic reasoning through a large vision-language model (VLM) [2]. SAP infers the shared visual or semantic concept between the inputs and synthesizes an anchor-prompt that encapsulates their semantic intersection. This prompt serves as a semantic anchor during denoising, guiding the diffusion process toward contextually plausible and semantically bridged transitions. Together, ACI and SAP enable CHIMERA to produce morphing sequences that remain visually natural and semantically coherent, even across disparate two visual domains. Finally, we pro-



pose the Global-Local Consistency Score (GLCS), the first morphing-oriented evaluation metric designed to quantitatively assess transition quality. GLCS measures semantic consistency, temporal smoothness, and contextual plausibility, providing a principled and quantitative basis for evaluating morphing quality, also well aligned with user study. Our contributions are as follows:

- **CHIMERA**: A zero-shot diffusion morphing framework based on cached inversion-guided denoising, achieving structurally semantic alignment in training-free manner.
- **Adaptive Cache Injection (ACI)**: Adaptively re-injects cached inversion features in a depth- and timestep-adaptive manner, stabilizing feature fusion and yielding smooth morphing transitions.
- **Semantic Anchor Prompting (SAP)**: Leverages a shared high-level anchor-prompt inferred from the two inputs, effectively bridging semantics between them and reducing drift for heterogeneous pairs.
- **Global-Local Consistency Score (GLCS)**: A new morphing-oriented metric that jointly quantifying the global harmonization and the smoothness of the local transition.

## 2. Related Work

### 2.1. Image Morphing

Image morphing is a long-standing task in computer vision and graphics [1, 50, 60], aiming to generate perceptually smooth transitions between two images. Early methods [3, 26, 50] rely on geometric correspondences such as feature-line interpolation or optical-flow-based warping [6, 21]. While effective for small deformations, these techniques often produce ghosting artifacts or distorted in-betweens when facing large appearance or semantic gaps. Tuning-based approaches [30, 38] attempt to model morphing as a data-driven transformation, yet their reliance on class-specific training data limits generalization across diverse categories and domains.

With the rise of diffusion-based generation, recent works [7, 24, 27, 49] formulate morphing as interpolation in latent space. DiffMorpher [27] and IMPUS [24] fine-tune diffusion models to achieve smooth transitions, whereas FreeMorph [7] performs in training-free manner via DDIM inversion [32]. These methods demonstrate the strength of diffusion priors as a powerful backbone, yet still face challenges in maintaining semantic coherence and cross-domain consistencies due to their lack of adaptive mechanisms and the absence of dedicated components for handling highly heterogeneous input pairs. As a result, the denoising diffusion process cannot dynamically adjust to structural or semantic disparities, often leading to visually inconsistent or domain-biased results.

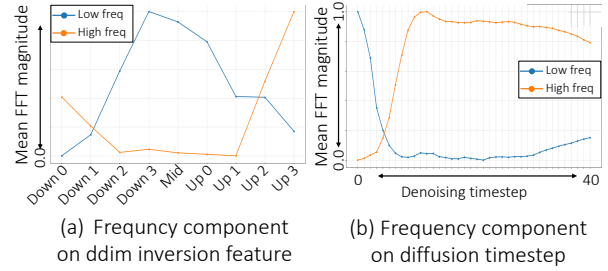


Figure 3. **Frequency analysis of diffusion features and denoising timesteps.** Low- (blue) and high-frequency (orange) components across (a) U-Net feature layers and (b) DDIM denoising timesteps are measured for the base model without CHIMERA’s ACI and SAP on Morph4Data [7]. Values are obtained by applying FFT with masked frequency bands and averaging the resulting magnitudes.

### 2.2. Diffusion Latents and Feature Reuse

Diffusion models [13, 19, 44] iteratively denoise latent variables, forming hierarchical multi-scale features within a U-Net architecture [40]. Intermediate representations capture both geometric and semantic cues [23, 36], enabling controllable interpolation in latent space. Several works leverage these internal states for generation stability and control, including classifier-free guidance [18], self-conditioning [11], and adapter-based modulation [46, 56]. Feature reuse and attention modulation techniques [16, 28] further enhance spatial coherence and mitigate over-saturation. Our work follows this direction by employing feature-level guidance to preserve structural stability for morphing.

### 2.3. Text-guided Diffusion Models

Vision–Language Models (VLMs) [2, 31, 37] align textual and visual semantics in a shared embedding space. This property has been widely adopted to control diffusion-based generation via semantic interpolation or additive manipulation [34]. Cross-attention [8, 55] has emerged as an effective mechanism for regulating semantic consistency during denoising, revealing text tokens as high-level controllers. In this context, our approach integrates such strong VLM priors into diffusion models to achieve semantically coherent morphing across diverse domains.

## 3. Preliminaries and Observations

**Denoising Diffusion Implicit Models (DDIM).** The Denoising Diffusion Implicit Model (DDIM) [43] defines a deterministic generative process that maps Gaussian noise to a clean image through a sequence of denoising steps. Given an input noise sample  $x_T$ , DDIM reconstructs an image  $x_0$

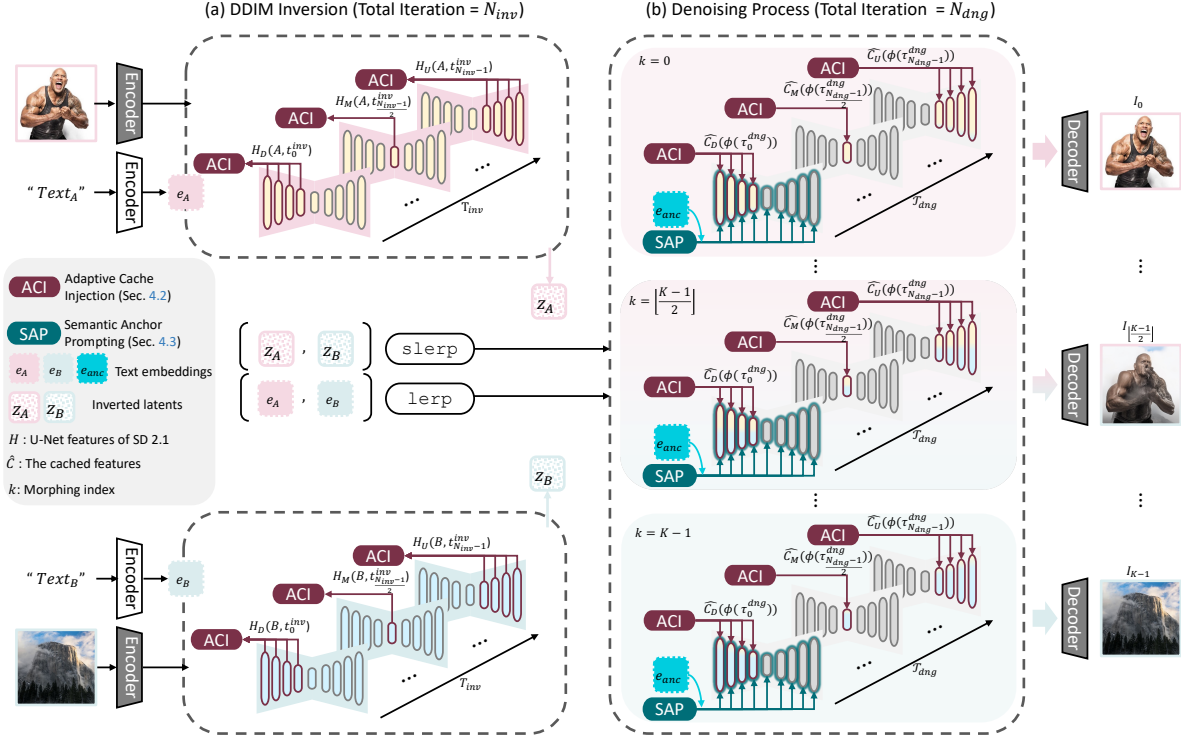


Figure 4. **Overview of the CHIMERA framework.** (a) DDIM Inversion: Inputs  $A$  and  $B$  are inverted while caching multi-scale U-Net features from the down, mid, and up blocks. The cached features are interpolated via  $\text{slerp}$ , forming morphing-aligned latents. (b) Denoising: The interpolated caches are re-injected through ACI, which aligns inversion and denoising timesteps via the proposed IDM. ACI injects mid-block features at early steps (low-frequency structure) and up-block features at later steps (high-frequency refinement). In parallel, SAP introduces a VLM-derived anchor-prompt into early cross-attention layers, stabilizing semantics and reducing drift for heterogeneous pairs. The full algorithm is provided in Algorithm 1 of the Suppl.

by iteratively updating the latent variable  $x_t$  as:

$$x_{t-1} = \sqrt{\bar{\alpha}_{t-1}} \left( \frac{x_t - \sqrt{1 - \bar{\alpha}_t} \epsilon_\theta(x_t, t)}{\sqrt{\bar{\alpha}_t}} \right) + \sqrt{1 - \bar{\alpha}_{t-1}} \epsilon_\theta(x_t, t). \quad (1)$$

where  $\epsilon_\theta$  denotes the predicted noise at timestep  $t$ , and  $\bar{\alpha}_t$  controls the variance schedule. The deterministic formulation of DDIM also enables inversion, where a real image  $x_0$  can be projected into its corresponding latent trajectory by reversing the forward diffusion process. In our framework, these inverted latents from both input images serve as the initial states for morphing. By interpolating between them, we initiate the denoising process from structured latent priors, allowing the model to generate smooth and coherent transitions without retraining the diffusion backbone.

**Observation.** Before introducing Adaptive Cache Injection (ACI), we analyze the diffusion features (of Stable Diffusion 2.1 [39]) from DDIM inversion and the denoising timesteps from a frequency-domain perspective. This analysis allows us to match components with similar frequency characteristics between the DDIM inversion features and

the denoising timesteps, which in turn improves the overall morphing performance. As shown in Fig. 3 (a) features closer to the mid layers tend to emphasize low-frequency components, while features closer to the up layers emphasize high-frequency components. Likewise, Fig. 3 (b) indicates that early denoising timesteps are dominated by low-frequency structure, whereas later timesteps emphasize high-frequency details. Guided by these observations, we inject features from layers near the mid block in the early timesteps and features from layers near the up block in the later timesteps. Detailed qualitative and quantitative studies are provided in Sec. 5.3.1.

## 4. Proposed Method: CHIMERA

**Overall Pipeline.** As shown in Fig. 4, Given input images  $A$  and  $B$ , we first project them into the latent space using a DDIM inversion (DDIM) [43] to obtain  $z_A = \text{DDIM}(A)$  and  $z_B = \text{DDIM}(B)$ . We then perform spherical interpolation ( $\text{slerp}$ ) to form the  $K$ -morphing latent images:

$$z_k = \text{slerp}(z_A, z_B; \alpha_k), \quad k = 0, \dots, K-1, \quad (2)$$

where  $\alpha_k$  denotes the interpolation weight used to traverse between  $z_A$  and  $z_B$ ,  $K$  is the number of intermediate morphing latents and  $k$  denotes index of `slerp`.

During DDIM inversion [52] to obtain the inverted latents for  $A$  and  $B$ , we cache multi-scale U-Net features. Specifically, we record the down, mid, and up features as:

$$H_S(X, t), \quad S \in \{\mathbf{D}, \mathbf{M}, \mathbf{U}\}, X \in \{A, B\}, t \in T_{\text{inv}}, \quad (3)$$

where  $H_S$  denotes the multi-scale U-Net features and  $\mathbf{D}, \mathbf{M}, \mathbf{U}$  represent downsampling, mid, and upsampling blocks. Here,  $T_{\text{inv}} = (t_0^{\text{inv}}, \dots, t_{N_{\text{inv}}-1}^{\text{inv}})$  denotes the set of inversion timesteps with the total number of  $N_{\text{inv}}$ -inversion timestep. We then apply `slerp` to the cached features:

$$\hat{C}_S(k, t) = \text{slerp}(H_S(A, t), H_S(B, t); \alpha_k), \quad (4)$$

where  $\hat{C}_S(k, t)$  denotes interpolated cached U-Net feature,  $k$  denotes index of `slerp` and  $t$  denotes timestep of DDIM. These interpolated features are subsequently injected into the U-Net during denoising according to their matched timesteps.

#### 4.1. Adaptive Cache Injection (ACI)

Previous image morphing methods [7, 24, 27] typically interpolate only the latents obtained from DDIM and then perform denoising. However, prior state-of-the-art (SOTA) method [7] provides limited input-aligned guidance to the diffusion model, often producing images that deviate from both  $A$  and  $B$ . To address this limitation, we propose **Adaptive Cache Injection (ACI)**, which guides the denoising process by injecting depth- and timestep-adaptive cached multi-scale features.

As described in Sec. 4, during DDIM, we cache down ( $\mathbf{D}$ ), mid ( $\mathbf{M}$ ), and up ( $\mathbf{U}$ ) features for each input (see Eq. 3). Then, for each morphing index  $k$ , cached features from  $A$  and  $B$  are blended via Eq. 4.

To inject these features during denoising, we map the denoising step  $\tau$  to an inversion timestep. Let  $T_{\text{dng}} = (\tau_0^{\text{dng}}, \dots, \tau_{N_{\text{dng}}-1}^{\text{dng}})$  denote the sampling (denoising) timesteps with total  $N_{\text{dng}}$  steps.

If the relationship between the inversion timestep obtained in Eq. 4 and the denoising timestep  $\tau$  is not considered, a timestep mismatch may occur, causing unwanted structures or excessive oversmoothing (see *Suppl.* for more details). To address this issue, we propose the **Inversion-Denoising Timestep Mapping (IDM)**, a function that maps the DDIM inversion timestep  $t$  to the denoising timestep  $\tau$  as follow:

$$t = \phi(\tau), \quad \phi(\tau) = T_{\text{inv}} \left[ \text{round} \left( \frac{\tau}{N_{\text{dng}} - 1} (N_{\text{inv}} - 1) \right) \right], \quad \tau \in \{0, \dots, N_{\text{dng}} - 1\}, \quad (5)$$

where  $\phi$  denotes the IDM,  $[\cdot]$  denotes square-bracket indexing notation and `round` denotes rounding to the nearest integer. The blended cached feature used at denoising step  $\tau$  becomes:

$$\hat{C}_S(k, \phi(\tau)) = \text{slerp}(H_S(A, \phi(\tau)), H_S(B, \phi(\tau)); \alpha_k). \quad (6)$$

The cached feature  $\hat{C}_S$  is multiplied by the blending weight  $\lambda_S$  and then added as a residual:

$$\tilde{F}_S^{(\tau)} = F_S^{(\tau)} + \lambda_S \cdot \hat{C}_S(\phi(\tau)), \quad (7)$$

where  $F_S$  denotes the denoising diffusion feature at layer  $S$ , and  $\tilde{F}_S$  represents the feature after adding the cached feature as a residual. Through this overall process, ACI provides layer-wise, aligned timestep-aware guidance, enabling the generation of smooth and faithful morphing results aligned with both  $A$  and  $B$ .

#### 4.2. Semantic Anchor Prompting (SAP)

We further address the problem of abrupt transitions and unreasonable intermediate images that often arise when the correspondence between two input images is ambiguous. To this end, we propose **Semantic Anchor Prompting (SAP)**, which leverages a VLM (e.g., Qwen2.5-VL [2]) to infer a shared high-level concept encapsulating the common semantic or layout between the two inputs. The resulting *anchor-prompt* acts as an anchor that stabilizes the denoising process, guiding the model to generate consistent morphing results.

**Anchor-Prompt.** We query a VLM [2] with a structured anchor-prompt that outputs (1) a concise phrase describing their *shared semantic or structural concept*, and (2) two factual text prompts that naturally reflect this shared concept. Since both text prompts are generated with reference to the anchor-prompt, they inherently encode overlapping semantics either explicitly through keyword repetition or implicitly through conceptual alignment. This design induces stronger textual correlation between the two inputs, facilitating smoother interpolation in the subsequent attention operations. We denote the anchor-prompt and two text prompts as  $\text{text}_{\text{anc}}$ ,  $\text{text}_A$ , and  $\text{text}_B$ , respectively, and encode all of them via the CLIP text encoder [37] to obtain embeddings  $\mathbf{e}_{\text{anc}}$ ,  $\mathbf{e}_A$ , and  $\mathbf{e}_B$ . Given the approximately locally linear nature of CLIP’s embedding space [5, 24, 34], semantically related embeddings are positioned in close proximity, allowing more stable and meaningful blending within the denoising process. The full anchor-prompt template is provided in the *Suppl.*

**SAP Operation.** The anchor-prompt is incorporated within the all cross-attention layers [39], where textual semantics directly influence visual features. At denoising step, the three embeddings are projected into key-value



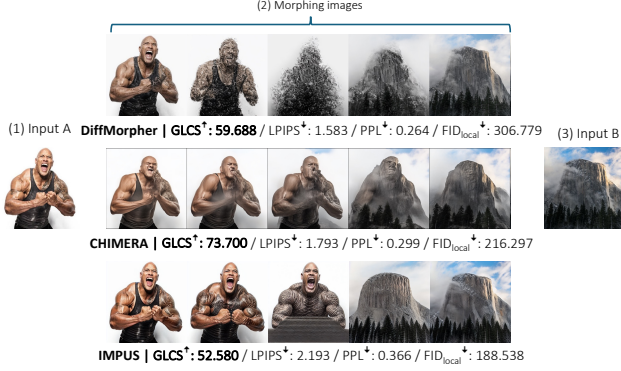


Figure 5. **Qualitative results of the proposed GLCS.** Given input image pairs (1) and (3), different methods produce morphing sequences shown in (2), which highlight cases where GLCS successfully reflects differences in global-local consistency that are not fully captured by conventional metrics.

pairs  $(K_A, V_A)$ ,  $(K_B, V_B)$ , and  $(K_{anc}, V_{anc})$ . The anchor projection is concatenated with each endpoint branch as follows:

$$\text{Attn}_X = \text{softmax}\left(\frac{Q[K_X \| K_{anc}]^T}{\sqrt{d}}\right) [V_X \| V_{anc}], \quad (8)$$

$$X \in \{A, B\}.$$

For semantically similar input pairs, the shared anchor-prompt provides complementary contextual cues that enrich fine-grained consistency, while for heterogeneous pairs, it mitigates semantic drift and promotes balanced blending across domains.

**Denoising Timestep-Aware Schedule.** SAP is activated only during early denoising timesteps as shown in Sec. 4, where the diffusion model establishes the coarse global structure and semantic layout. Empirically, extending semantic conditioning to later stages was found to introduce over-smoothing or hallucinations, while restricting SAP to the early stage consistently yielded the most stable and smooth transitions. The complete algorithmic formulation is provided in the *Suppl.*

### 4.3. Global-Local Consistency Score (GLCS)

**Motivation.**  $\text{FID}_{\text{local}}$  [17],  $\text{FID}_{\text{global}}$  [17], LPIPS [57], and PPL [22] are commonly used for quantitative evaluation for image morphing task (see Fig. 5). However, these metrics are not aligned with human perception of morphing quality. LPIPS and PPL only measure the similarity between adjacent images, and thus sequences that deviate from the input images  $A$  and  $B$  may still obtain low scores as long as nearby images remain similar. For example, in Fig. 5 (2), the first row yields lower LPIPS and PPL values than the second row, even though the latter is visually superior.  $\text{FID}_{\text{local}}$  also fails to reflect perceptual domain consistency because it averages the distribution gap between

$A, B$  and all morphing images without considering the interpolation ratio. Consequently, it often favors images that resemble both inputs simultaneously rather than those forming a natural transition. As shown in Fig. 5 (2),  $\text{FID}_{\text{local}}$  incorrectly prefers the third row over the second, despite the second showing clearer preservation of domain characteristics (e.g., stone texture and facial identity). To address these perceptual limitations, we propose the **Global-Local Consistency Score (GLCS)**, which jointly evaluates domain consistency and smoothness in a morphing-aware manner.

**Proposed Metric.** We propose **Global-Local Consistency Score** to evaluate morphing quality with two complementary factors. First, the **Global Consistency Score (GCS)** measures domain consistency. It checks whether each image follows the expected global trend between the two input images  $A$  and  $B$ . We obtain this trend by interpolating the endpoint similarities with `slerp`, so the sequence should change in a balanced way from  $A$  to  $B$ . Second, the **Local Consistency Score (LCS)** measures **smoothness**. It checks whether the similarity of each image changes smoothly with respect to its neighbors. Thus, LCS captures local continuity along the morphing transition. We use a DiffSim-based [45] bounded similarity  $s(\cdot, \cdot)$ , which is sensitive to low-level structure and also reflects style and semantic similarity. Both GCS and LCS are clamped to  $[0, 1]$  for stability and interpretability. GLCS combines these two perspectives and is high only when the sequence is globally well-mixed and locally smooth:

$$\text{GLCS} = \sqrt{\text{GCS} \cdot \text{LCS}}. \quad (9)$$

For a detailed description of GLCS and the corresponding qualitative results, please refer to the *Suppl.*

## 5. Experiment

**Implementation Detail.** Our proposed model, CHIMERA, is based on the diffusion model Stable Diffusion 2.1 [39]. For ACI, we use  $N_{\text{inv}} = 50$  DDIM inversion timesteps and  $N_{\text{dng}} = 50$  denoising timesteps. The cached layers mentioned in Eq. 7 are weighted with  $\lambda_S = 0.4$ . The classifier guidance strength and image resolution are set to 0.75 and  $768 \times 768$  respectively, following FreeMorph [7]. Further implementation details are provided in the *Suppl.* for reproducibility.

**Evaluation Datasets.** MorphBench [27] is a benchmark for evaluating image morphing on general objects, consisting of 90 image pairs spanning object metamorphosis and animation-based continuous transformations. Morph4Data [7] complements MorphBench by providing broader semantic and layout diversity, including pairs with similar layouts but different semantics, pairs with aligned semantics (e.g., human faces and cars), randomly sampled ImageNet-1K [41] pairs, and dog-cat pairs collected from the internet.

Morph4Data						MorphBench					User-study	
Model name	FID <sub>local</sub> ↓	FID <sub>global</sub> ↓	LPIPS↓	PPL↓	GLCS↑	Model name	FID <sub>local</sub> ↓	FID <sub>global</sub> ↓	LPIPS↓	PPL↓	GLCS↑	Overall Quality↑
IMPUS	<b>150.1332</b>	<b>70.231</b>	1.912	0.319	81.902	IMPUS	<b>93.417</b>	<b>44.287</b>	1.296	0.216	89.426	3.11 ± 2.11
DiffMorpher	181.992	92.548	<b>1.638</b>	<b>0.273</b>	85.156	DiffMorpher	133.086	62.127	<b>1.044</b>	<b>0.174</b>	<b>91.887</b>	<b>3.43 ± 1.34</b>
FreeMorph	191.348	98.444	1.973	0.329	<b>86.641</b>	FreeMorph	148.972	81.019	1.494	0.249	90.566	2.92 ± 1.21
CHIMERA	<b>171.731</b>	<b>87.852</b>	<b>1.661</b>	<b>0.277</b>	<b>88.616</b>	CHIMERA	<b>128.223</b>	<b>68.405</b>	<b>1.129</b>	<b>0.188</b>	<b>93.671</b>	<b>3.61 ± 1.14</b>

Table 1. **Quantitative comparison on Morph4Data and MorphBench.** Comparison of CHIMERA and baseline methods on Morph4Data and MorphBench in terms of conventional metrics and the proposed GLCS, with user study Overall Quality scores reported in the rightmost columns.

**Evaluation Metrics.** We conduct quantitative evaluation using the metrics adopted in prior methods [7, 24, 27], including FID<sub>local</sub> [17], FID<sub>global</sub> [17], LPIPS [57], PPL [22], and our proposed GLCS. For detailed definitions and evaluation protocols, please refer to the *Suppl.*

### 5.1. Quantitative Evaluations

Our quantitative evaluation follows previous image morphing methods [7, 24, 27] and includes FID<sub>global</sub>, FID<sub>local</sub>, LPIPS, and PPL, along with our proposed GLCS. As shown in Table 1, IMPUS achieves the best performance on FID<sub>local</sub> and FID<sub>global</sub> for both Morph4Data and MorphBench. However, its LPIPS and PPL scores, which measure smoothness, are poor, and its GLCS score (evaluating both domain consistency and smoothness) is also low. This indicates that IMPUS produces many abrupt transitions along the morphing trajectory. DiffMorpher shows the best LPIPS and PPL performance across both datasets, but its performance on FID<sub>local</sub>, FID<sub>global</sub>, and GLCS is worse. This occurs because DiffMorpher focuses heavily on generating smooth transitions while ignoring domain consistency and perceptual quality. FreeMorph performs poorly across all four metrics (FID<sub>local</sub>, FID<sub>global</sub>, LPIPS, PPL). This degradation stems from its inability to address the inherent over-smoothing and excessive color saturation often found in diffusion models, leading to low domain consistency and low smoothness. Interestingly, FreeMorph shows comparable performance to DiffMorpher in GLCS. This is because, although its domain consistency is low, its smoothness (measured by considering interpolation ratios between adjacent frames) is relatively high. Our proposed CHIMERA achieves performance comparable to tuning-based methods such as IMPUS and DiffMorpher across FID<sub>local</sub>, FID<sub>global</sub>, LPIPS, and PPL, while significantly outperforming the zero-shot method FreeMorph by a large margin. Moreover, CHIMERA achieves SOTA GLCS scores on both datasets. These results demonstrate that CHIMERA delivers high performance in terms of domain consistency, smoothness, and perceptual quality. In addition, we conducted a user study across four perceptual criteria. As shown in Table 1 where CHIMERA was consistently preferred over all baselines, further validating its practical effectiveness. Detailed user study results are provided in the *Suppl.*

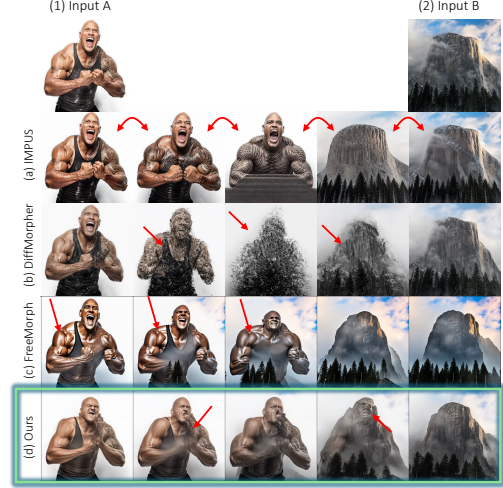


Figure 6. **Qualitative comparisons with existing SOTA methods.** (1)–(2) denote the input image pairs. (a)–(d) show qualitative results for each model on the Morph4Data dataset.

### 5.2. Qualitative Evaluations

To demonstrate the effectiveness of our proposed CHIMERA, we provide a qualitative comparison with existing methods in Fig. 6. As shown by the red arrows in Fig. 6 (a), the transition is relatively natural near the input images *A* and *B*, but it becomes increasingly abrupt toward the center of the sequence. As observed in the red arrows of Fig. 6 (b), DiffMorpher loses semantic information from both *A* and *B* when the input pair becomes more dissimilar, leading to degraded perceptual quality. In Fig. 6 (c), FreeMorph achieves good perceptual quality and smoothness but still introduces saturated colors and over-smoothing, producing textures that deviate from the input pair. In contrast, CHIMERA preserves perceptual quality while maintaining the semantics of both *A* and *B*, achieving smooth transitions. Notably, in Fig. 6 (d), the red arrows show that our model retains the stone texture on the person’s arm and coherently blends the person’s face into the rocky mountain. Additional visual comparisons are provided in the *Suppl.*

ACI Ablation – layer type						
	layer	FID <sub>local</sub> ↓	FID <sub>global</sub> ↓	LPIPS↓	PPL↓	GLCS↑
(a)	{D}	<u>181.705</u>	<u>92.185</u>	1.801	0.300	87.904
(b)	{D, M}	181.812	92.350	1.799	0.300	87.886
(c)	{D, M, U} (Ours)	<b>173.248</b>	<b>89.064</b>	<b>1.666</b>	<b>0.278</b>	<b>89.592</b>
(d)	{M, U}	200.795	99.208	<u>1.765</u>	<u>0.294</u>	86.230
(e)	{U}	199.945	99.544	1.772	0.295	<u>88.337</u>

Table 2. **Quantitative evaluation based on the types of caching layers used in ACI.** D, M, and U denote the down, mid, and up layers extracted during the DDIM inversion process, respectively.

ACI Ablation – layer weight						
	$\lambda_S$	FID <sub>local</sub> ↓	FID <sub>global</sub> ↓	LPIPS↓	PPL↓	GLCS↑
(a)	0.1	185.647	93.810	1.818	0.303	88.152
(b)	0.4 (Ours)	<b>173.248</b>	<b>89.064</b>	1.666	0.278	<b>89.592</b>
(c)	0.7	<u>175.312</u>	<u>90.711</u>	<u>1.562</u>	<u>0.260</u>	88.774
(d)	1.0	200.280	103.238	<b>1.521</b>	<b>0.254</b>	<u>88.790</u>

Table 3. **Impact of injection weights in ACI.** Quantitative evaluation with respect to the injection weight ( $\lambda_S$ ) of the caching layers in ACI.



Figure 7. **Qualitative results based on the types of features cached in ACI.** (i) and (ii) represent the input image pair, while D, M, and U denote the down, mid, and up features, respectively.

### 5.3. Ablation Studies

#### 5.3.1. Caching Feature Type on ACI

When only the down or down-mid features are provided, as shown in Fig. 7 (a) and (b) (red arrow), the results tend to lose fine details and exhibit surface oversmoothing. This suggests that the up layers, which contain rich high-frequency information, should be included. Conversely, when only the up or mid-up features are used, as observed in the first and second columns of Fig. 7 (d) and (e) (red arrow) where the arm disappears, it indicates that the down

SAP Ablation – injection timestep					
	FID <sub>local</sub> ↓	FID <sub>global</sub> ↓	LPIPS↓	PPL↓	GLCS↑
(a) stage1	<b>171.7308</b>	<b>87.8516</b>	1.6607	0.2768	<b>89.016</b>
(b) stage2	<u>200.7918</u>	<u>102.1788</u>	<b>1.5647</b>	<b>0.2608</b>	<u>88.7686</u>
(c) stage1+stage2	215.8786	107.9795	<u>1.6299</u>	<u>0.2716</u>	88.439

Table 4. **Ablation on the SAP injection schedule.** stage1 and stage2 denote applying SAP in the early stage and in the late stage of the denoising process, respectively.

and mid blocks, which provide abundant low-frequency semantic information, are essential for improving the overall perceptual quality. As shown in Table 2, our model, which uses all down, mid, and up blocks, achieves the best performance across all evaluation metrics.

#### 5.3.2. Caching Injection Weight of ACI

In Table 3, we provide the quantitative evaluation of the injection weight. We set  $\lambda_S$  as 0.4, it achieves the best FID scores. Although the LPIPS and PPL values are relatively higher, we choose  $\lambda_S = 0.4$  as the final weight because GLCS offers a more reliable assessment of smoothness. Additional qualitative results are provided in the *Suppl.*

#### 5.3.3. Schedule for SAP operation

We divide the denoising process into two stages: an early coarse-to-mid structural stage and a late high-frequency refinement stage. Following prior work [7], the late stage remains fixed. As shown in Table 4, applying SAP only in the early stage achieves the best consistency and fidelity. Using SAP in the second stage or across both stages degrades performance, indicating that semantic cues are most effective before high-frequency refinement. Therefore, CHIMERA adopts a first-stage-only SAP schedule, which consistently yields the most stable morphing trajectories.

## 6. Conclusion

We have presented CHIMERA, a zero-shot diffusion-based framework that has achieved smooth, semantically coherent, and domain-consistent image morphing. Through Adaptive Cache Injection (ACI) and Semantic Anchor Prompting (SAP), our method has effectively guided the denoising process using both multi-scale inversion features and VLM-derived semantic anchors. These components have mitigated over-smoothing, over-saturation, and semantic drift that prior morphing methods have suffered from. We have additionally proposed GLCS, a morphing-oriented metric that has aligned closely with human perceptual judgment. Extensive experiments and a user study have shown that CHIMERA consistently outperforms existing approaches. Overall, our framework has advanced zero-shot morphing and established a new SOTA in diffusion-based transformations.



## References

- [1] Alyaa Qusay Aloraibi. Image morphing techniques: A review. *Technium*, 9, 2023. 3
- [2] Shuai Bai, Keqin Chen, Xuejing Liu, Jialin Wang, Wenbin Ge, Sibao Song, Kai Dang, Peng Wang, Shijie Wang, Jun Tang, et al. Qwen2. 5-vl technical report. *arXiv preprint arXiv:2502.13923*, 2025. 2, 3, 5, 13, 15
- [3] Thaddeus Beier and Shawn Neely. Feature-based image metamorphosis. *ACM SIGGRAPH Computer Graphics*, 26(2):35–42, 1992. 3
- [4] Bhumika G Bhatt. Comparative study of triangulation based and feature based image morphing. *Signal & Image Processing*, 2(4):235, 2011. 2
- [5] Manuel Brack, Felix Friedrich, Dominik Hintersdorf, Lukas Struppek, Patrick Schramowski, and Kristian Kersting. Sega: Instructing text-to-image models using semantic guidance. *Advances in Neural Information Processing Systems*, 36: 25365–25389, 2023. 5
- [6] Thomas Brox, Andres Bruhn, Nils Papenberg, and Joachim Weickert. High accuracy optical flow estimation based on a theory for warping. In *European Conference on Computer Vision (ECCV)*, pages 25–36, 2004. 3
- [7] Jiayi Cao, Xinyu Lin, Yichen Xu, Jing Xu, Zhen Zhang, and Zongwei Li. Freemorph: Tuning-free generalized image morphing with diffusion models. *Proceedings of the IEEE/CVF Conference on Computer Vision and Pattern Recognition (CVPR)*, 2025. 1, 2, 3, 5, 6, 7, 8, 13, 14, 15, 17, 18
- [8] Hila Chefer, Ron Mokady, Or Lang, Yuval Alaluf, Gal Chechik, and Daniel Cohen-Or. Attention interpolation for text-to-image diffusion models. *Proceedings of the IEEE/CVF International Conference on Computer Vision (ICCV)*, 2023. 3
- [9] Jingye Chen, Yupan Huang, Tengchao Lv, Lei Cui, Qifeng Chen, and Furu Wei. Textdiffuser: Diffusion models as text painters. *Advances in Neural Information Processing Systems*, 36:9353–9387, 2023. 19
- [10] Jingxi Chen, Brandon Y Feng, Haoming Cai, Tianfu Wang, Levi Burner, Dehao Yuan, Cornelia Fermüller, Christopher A Metzler, and Yiannis Aloimonos. Repurposing pre-trained video diffusion models for event-based video interpolation. In *Proceedings of the Computer Vision and Pattern Recognition Conference*, pages 12456–12466, 2025. 17
- [11] Ting Chen, Ruixiang Zhang, and Martin Arjovsky. Improving diffusion models with self-conditioning. *Proceedings of the International Conference on Machine Learning (ICML)*, 2023. 3
- [12] Xianhang Cheng and Zhenzhong Chen. Multiple video frame interpolation via enhanced deformable separable convolution. *IEEE Transactions on Pattern Analysis and Machine Intelligence*, 44(10):7029–7045, 2021. 17
- [13] Prafulla Dhariwal and Alex Nichol. Diffusion models beat gans on image synthesis. In *Advances in Neural Information Processing Systems (NeurIPS)*, 2021. 3
- [14] Yutang Feng, Sicheng Gao, Yuxiang Bao, Xiaodi Wang, Shumin Han, Juan Zhang, Baochang Zhang, and Angela Yao. Wave: Warping ddim inversion features for zero-shot text-to-video editing. In *European Conference on Computer Vision*, pages 38–55. Springer, 2024. 2
- [15] Agus Gunawan, Samuel Teodoro, Yun Chen, Soo Ye Kim, Jihyong Oh, and Munchurl Kim. Omnitext: A training-free generalist for controllable text-image manipulation. *arXiv preprint arXiv:2510.24093*, 2025. 19
- [16] Amir Hertz, Ron Mokady, Jonathan B. Tenenbaum, Antonio Torralba, and Ariel Shamir. Prompt-to-prompt image editing with cross-attention control. *arXiv preprint arXiv:2208.01626*, 2022. 3
- [17] M. Heusel, Hubert Ramsauer, Thomas Unterthiner, Bernhard Nessler, and Sepp Hochreiter. Gans trained by a two time-scale update rule converge to a local nash equilibrium. In *Neural Information Processing Systems*, 2017. 6, 7
- [18] Jonathan Ho and Tim Salimans. Classifier-free diffusion guidance. In *Advances in Neural Information Processing Systems (NeurIPS)*, 2022. 3
- [19] Jonathan Ho, Ajay Jain, and Pieter Abbeel. Denoising diffusion probabilistic models. In *Advances in Neural Information Processing Systems (NeurIPS)*, 2020. 3
- [20] Seongmin Hong, Kyeonghyun Lee, Suh Yoon Jeon, Hyewon Bae, and Se Young Chun. On exact inversion of dpm-solvers. In *Proceedings of the IEEE/CVF Conference on Computer Vision and Pattern Recognition*, pages 7069–7078, 2024. 2
- [21] Berthold K.P. Horn and Brian G. Schunck. Determining optical flow. *Artificial Intelligence*, 17(1-3):185–203, 1981. 3
- [22] Tero Karras, S. Laine, M. Aittala, Janne Hellsten, J. Lehtinen, and Timo Aila. Analyzing and improving the image quality of stylegan. In *Computer Vision and Pattern Recognition*, 2019. 1, 6, 7
- [23] Jonghyun Kim, Jaehyung Park, Seungho Yang, and Dongyoon Han. Probability density geodesics in image diffusion latent space. *Proceedings of the IEEE/CVF Conference on Computer Vision and Pattern Recognition (CVPR)*, 2024. 3
- [24] Minjun Kim, Dahyeon Kye, Sukhun Ko, Hyeonjun Sim, and Sanghyun Park. Impus: Image morphing with perceptually uniform sampling using diffusion models. *Proceedings of the IEEE/CVF Conference on Computer Vision and Pattern Recognition (CVPR)*, 2024. 2, 3, 5, 7, 13, 15, 17, 18
- [25] Dahyeon Kye, Changhyun Roh, Sukhun Ko, Chanho Eom, and Jihyong Oh. Acevfi: A comprehensive survey of advances in video frame interpolation. *arXiv preprint arXiv:2506.01061*, 2025. 17
- [26] Sangho Lee and Hanseok Kim. Flow-based image morphing. *IEEE Transactions on Image Processing*, 21(2):820–833, 2012. 3
- [27] Hao Li, Zhihui Zhu, Ping Luo, and Yufeng Zhang. Diffmorpher: Unleashing the capability of diffusion models for image morphing. *Proceedings of the IEEE/CVF International Conference on Computer Vision (ICCV)*, 2023. 1, 2, 3, 5, 6, 7, 13, 15, 17, 18
- [28] Wenqi Li, Jingyu Zhao, Yifan Zhang, and Liwei Wang. Layer control: Revisiting layer-wise feature modulation for diffusion models. *arXiv preprint arXiv:2404.12217*, 2024. 3
- [29] Chunxu Liu, Guozhen Zhang, Rui Zhao, and Limin Wang. Sparse global matching for video frame interpolation with large motion. In *Proceedings of the IEEE/CVF conference*

- on computer vision and pattern recognition, pages 19125–19134, 2024. 17
- [30] Haoran Liu, Xiaolong Wang, and Lei Zhang. Neural image morphing for cross-domain transitions. In *European Conference on Computer Vision (ECCV)*, pages 401–418, 2022. 3
- [31] Haotian Liu, Chunyuan Li, Qingyang Wu, and Yong Jae Lee. Visual instruction tuning. *Advances in neural information processing systems*, 36:34892–34916, 2023. 3, 13
- [32] Ron Mokady, Amir Hertz, Kfir Aberman, Yael Pritch, and Daniel Cohen-Or. Null-text inversion for editing real images using guided diffusion models. In *Proceedings of the IEEE/CVF conference on computer vision and pattern recognition*, pages 6038–6047, 2023. 2, 3, 13
- [33] Simon Niklaus and Feng Liu. Softmax splatting for video frame interpolation. In *Proceedings of the IEEE/CVF conference on computer vision and pattern recognition*, pages 5437–5446, 2020. 17
- [34] Or Patashnik, Zongze Wu, Eli Shechtman, Daniel Cohen-Or, and Dani Lischinski. Styleclip: Text-driven manipulation of stylegan imagery. In *Proceedings of the IEEE/CVF international conference on computer vision*, pages 2085–2094, 2021. 3, 5
- [35] Jordi Pont-Tuset, Federico Perazzi, Sergi Caelles, Pablo Arbeláez, Alex Sorkine-Hornung, and Luc Van Gool. The 2017 davis challenge on video object segmentation. *arXiv preprint arXiv:1704.00675*, 2017. 17
- [36] Ben Poole, Ajay Jain, Jonathan T. Barron, and Ben Mildenhall. Dreamfusion: Text-to-3d using 2d diffusion. In *Advances in Neural Information Processing Systems (NeurIPS)*, 2023. 3
- [37] Alec Radford, Jong Wook Kim, Chris Hallacy, Aditya Ramesh, Gabriel Goh, Sandhini Agarwal, Girish Sastry, Amanda Askell, Pamela Mishkin, Jack Clark, Gretchen Krueger, and Ilya Sutskever. Learning transferable visual models from natural language supervision. *Proceedings of the International Conference on Machine Learning (ICML)*, 2021. 3, 5
- [38] Aleksa Rajković and Laurent Younes. Riemannian morphing on manifolds. In *International Conference on Computer Vision (ICCV)*, pages 1–11, 2023. 3
- [39] Robin Rombach, Andreas Blattmann, Dominik Lorenz, Patrick Esser, and Björn Ommer. High-resolution image synthesis with latent diffusion models. In *Proceedings of the IEEE/CVF conference on computer vision and pattern recognition*, pages 10684–10695, 2022. 2, 4, 5, 6, 19
- [40] Olaf Ronneberger, Philipp Fischer, and Thomas Brox. U-net: Convolutional networks for biomedical image segmentation. In *International Conference on Medical image computing and computer-assisted intervention*, pages 234–241. Springer, 2015. 2, 3
- [41] Olga Russakovsky, Jia Deng, Hao Su, Jonathan Krause, Sanjeev Satheesh, Sean Ma, Zhiheng Huang, Andrej Karpathy, Aditya Khosla, Michael Bernstein, Alexander C. Berg, and Li Fei-Fei. ImageNet Large Scale Visual Recognition Challenge. *International Journal of Computer Vision (IJCV)*, 115(3):211–252, 2015. 6
- [42] Wonyong Seo, Jihyong Oh, and Munchurl Kim. Bimvfi: Bidirectional motion field-guided frame interpolation for video with non-uniform motions. In *Proceedings of the Computer Vision and Pattern Recognition Conference*, pages 7244–7253, 2025. 17
- [43] Jiaming Song, Chenlin Meng, and Stefano Ermon. Denoising diffusion implicit models. *arXiv preprint arXiv:2010.02502*, 2020. 2, 3, 4
- [44] Yang Song, Jascha Sohl-Dickstein, Diederik P. Kingma, Abhishek Kumar, Stefano Ermon, and Ben Poole. Score-based generative modeling through stochastic differential equations. *Proceedings of the International Conference on Learning Representations (ICLR)*, 2021. 3
- [45] Yiren Song, Xiaokang Liu, and Mike Zheng Shou. DiffSim: Taming diffusion models for evaluating visual similarity. In *Proceedings of the IEEE/CVF International Conference on Computer Vision*, pages 16904–16915, 2025. 6, 7, 8
- [46] Shengding Tang, Wei Wu, Yixin Zhang, Yichong Jiang, Xingjun Li, Chen Lin, Jiajun Wang, Shujian Huang, Kun Zhou, Dahua Lin, and Ping Luo. T2i-adapter: Learning adapters to dig out more controllable ability for text-to-image diffusion models. In *Proceedings of the IEEE/CVF Conference on Computer Vision and Pattern Recognition (CVPR)*, 2023. 3
- [47] Tian Wang, Polina Golland, and Joshua Tenenbaum. Diffusion-based image interpolation via denoising trajectory alignment. In *Advances in Neural Information Processing Systems (NeurIPS)*, 2024. 2
- [48] Xiaojuan Wang, Boyang Zhou, Brian Curless, Ira Kemelmacher-Shlizerman, Aleksander Holynski, and Steven M Seitz. Generative inbetweening: Adapting image-to-video models for keyframe interpolation. *arXiv preprint arXiv:2408.15239*, 2024. 17
- [49] Yuxin Wang, Wenguan Wang, and Yi Yang. Interpolating between images with diffusion models. *Proceedings of the IEEE/CVF Conference on Computer Vision and Pattern Recognition (CVPR)*, 2023. 2, 3
- [50] George Wolberg. Image morphing: A survey. *The Visual Computer*, 14(8-9):360–372, 1998. 3
- [51] Guangyang Wu, Xin Tao, Changlin Li, Wenyi Wang, Xiaohong Liu, and Qingqing Zheng. Perception-oriented video frame interpolation via asymmetric blending. In *Proceedings of the IEEE/CVF Conference on Computer Vision and Pattern Recognition*, pages 2753–2762, 2024. 17
- [52] Sihan Xu, Yidong Huang, Jiayi Pan, Ziqiao Ma, and Joyce Chai. Inversion-free image editing with natural language. *arXiv preprint arXiv:2312.04965*, 2023. 5
- [53] Tianfan Xue, Baian Chen, Jiajun Wu, Donglai Wei, and William T Freeman. Video enhancement with task-oriented flow. *International Journal of Computer Vision*, 127(8):1106–1125, 2019. 17
- [54] Weichao Zeng, Yan Shu, Zhenhang Li, Dongbao Yang, and Yu Zhou. Textctrl: Diffusion-based scene text editing with prior guidance control. *Advances in Neural Information Processing Systems*, 37:138569–138594, 2024. 19
- [55] Hanting Zhang, Yifan Deng, Yixiao Zhang, Xinyu Chen, Zhaoxi Li, Kaili Chen, Yifan Li, Pan Lu, Ping Luo, and

- Dengxin Dai. Free-lunch color-texture disentanglement for stylized image generation. *Proceedings of the IEEE/CVF Conference on Computer Vision and Pattern Recognition (CVPR)*, 2023. [3](#)
- [56] Lvmin Zhang, Maneesh Rao, and Maneesh Agrawala. Adding conditional control to text-to-image diffusion models. In *Proceedings of the IEEE/CVF Winter Conference on Applications of Computer Vision (WACV)*, 2023. [3](#)
- [57] Richard Zhang, Phillip Isola, Alexei A. Efros, Eli Shechtman, and Oliver Wang. The unreasonable effectiveness of deep features as a perceptual metric. In *2018 IEEE/CVF Conference on Computer Vision and Pattern Recognition*, 2018. [1](#), [6](#), [7](#)
- [58] Zihao Zhang, Haoran Chen, Haoyu Zhao, Guansong Lu, Yanwei Fu, Hang Xu, and Zuxuan Wu. Eden: Enhanced diffusion for high-quality large-motion video frame interpolation. In *Proceedings of the Computer Vision and Pattern Recognition Conference*, pages 2105–2115, 2025. [17](#)
- [59] Qilong Zhangli, Jindong Jiang, Di Liu, Licheng Yu, Xiaoliang Dai, Ankit Ramchandani, Guan Pang, Dimitris N Metaxas, and Praveen Krishnan. Layout-agnostic scene text image synthesis with diffusion models. In *2024 IEEE/CVF Conference on Computer Vision and Pattern Recognition (CVPR)*, pages 7496–7506. IEEE Computer Society, 2024. [19](#)
- [60] Bhushan Zope and Soniya B Zope. A survey of morphing techniques. *International Journal of Advanced Engineering, Management and Science*, 3(2):239773, 2017. [3](#)



# CHIMERA: Adaptive Cache Injection and Semantic Anchor Prompting for Zero-shot Image Morphing with Morphing-oriented Metrics

## Supplementary Material

### A. Extended Experiment Results

This section provides additional quantitative and qualitative evaluations that supplement Sec. 5.1 and Sec. 5.2. In Sec. A.1, we present qualitative and quantitative results for the setting where 14 morphing images are generated between input images  $A$  and  $B$ . Unlike Sec. 5.1, which reports quantitative results for the 5-image morphing setting, this section evaluates CHIMERA under a longer morphing transition to assess the general applicability of the proposed method. In addition, Sec. A.2 provides further qualitative results for the 5-frame morphing scenario discussed in Sec. 5.2.

#### A.1. Extended Evaluation on Challenging 14-Image Morphing

Table 5 reports the quantitative results for the setting where 14 morphing images are generated between each input image pair, which is a more challenging configuration than generating 5 morphing images as in Sec. 5.1. Similar to the observations in Sec. 5.1, IMPUS achieves the best scores in  $FID_{local}$  and  $FID_{global}$  on both datasets, but shows weaker performance in LPIPS, PPL, and GLCS. DiffMorpher obtains the best LPIPS and PPL scores, yet its performance in  $FID_{local}$ ,  $FID_{global}$ , and GLCS is relatively lower. FreeMorph shows degraded performance in all metrics except GLCS.

In contrast, the proposed CHIMERA demonstrates performance comparable to the fine-tuning-based models IMPUS and DiffMorpher across  $FID_{local}$ ,  $FID_{global}$ , LPIPS, and PPL, while achieving a significantly higher GLCS. Furthermore, compared to FreeMorph, which is also a zero-shot model, CHIMERA outperforms it by a large margin across all metrics.

Qualitatively, IMPUS maintains strong domain consistency in each generated image but lacks smooth transitions between frames. DiffMorpher produces smooth transitions but often introduces severe artifacts, leading to poor domain consistency. FreeMorph provides visually smooth transitions but suffers from overly saturated colors, which also reduces domain consistency. In contrast, CHIMERA achieves both smooth frame-to-frame transitions and strong domain consistency, making it superior across both qualitative and quantitative evaluations.

We additionally provide qualitative results for the setting with 14 morphing images in Fig. 10 and Fig. 11. Similar to Fig. 8 and Fig. 9, IMPUS shows transitions with insufficient smoothness, while DiffMorpher contains many frames

Morph4Data					
Model name	$FID_{local} \downarrow$	$FID_{global} \downarrow$	LPIPS $\downarrow$	PPL $\downarrow$	GLCS $\uparrow$
IMPUS	<b>120.8154</b>	<b>60.0457</b>	2.7373	0.1825	88.9437
DiffMorpher	175.4093	89.8695	<b>1.8747</b>	<b>0.125</b>	89.2115
FreeMorph	178.7923	94.0618	2.5384	0.1692	<u>90.1506</u>
CHIMERA	<u>163.0485</u>	<u>84.7038</u>	<u>1.9941</u>	<u>0.1329</u>	<b>91.499</b>

MorphBench					
Model name	$FID_{local} \downarrow$	$FID_{global} \downarrow$	LPIPS $\downarrow$	PPL $\downarrow$	GLCS $\uparrow$
IMPUS	<b>78.9435</b>	<b>40.8919</b>	1.5866	0.1058	93.679
DiffMorpher	90.7386	46.1755	<b>1.0505</b>	<b>0.07</b>	<u>94.814</u>
FreeMorph	141.7272	79.1784	1.7763	0.1184	92.412
CHIMERA	<u>121.9058</u>	<u>66.3192</u>	<u>1.2005</u>	<u>0.08</u>	<b>95.353</b>

Table 5. **Quantitative results for challenging 14-image morphing (compared to 5-image morphing).** We report the metrics for IMPUS, DiffMorpher, FreeMorph, and CHIMERA.

where the structure collapses. FreeMorph also produces images with overly saturated colors. In contrast, as shown in panels (d) and (h) of Fig. 10 and Fig. 11, CHIMERA consistently maintains both smooth transitions and strong domain consistency.

These qualitative results are consistent with the quantitative evaluations presented earlier. For example, IMPUS achieves high scores in  $FID_{local}$  and  $FID_{global}$ , which measure domain consistency, but shows lower performance in LPIPS and PPL, which assess smoothness. Conversely, DiffMorpher performs well in terms of smoothness but exhibits lower domain consistency.

#### A.2. Additional Qualitative Result on 5-Image Morphing

Fig. 8 and Fig. 9 present qualitative results for the setting where five morphing images are generated between  $A$  and  $B$ . As shown in panels (a) and (e) of Fig. 8 and Fig. 9 (red arrows), IMPUS produces frames with abrupt transitions. In panels (b) and (f), the morphing images exhibit good smoothness, but the red arrows highlight collapsed structures or noticeable artifacts. In panels (c) and (g), the transitions remain smooth, yet the red arrows indicate a tendency toward excessively saturated colors. In contrast, panels (d) and (h) of Fig. 8 and Fig. 9 show that the proposed CHIMERA preserves both domain consistency and smoothness.



Figure 8. **Qualitative comparison showing the results of generating five morphing images.** Panels (1)–(4) denote the input images, and panels (a)–(d) correspond to IMPUS, DiffMorpher, FreeMorph, and CHIMERA (Ours), respectively. The same convention applies to panels (e)–(h).

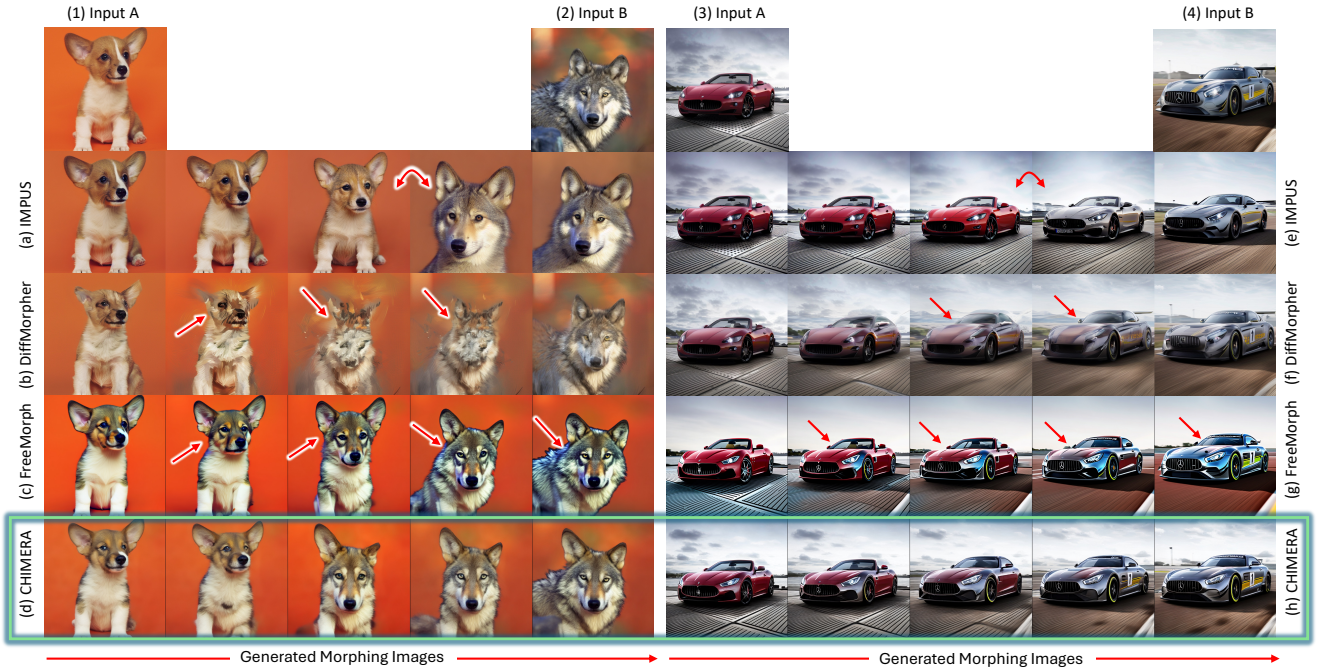


Figure 9. **Qualitative comparison showing the results of generating five morphing images.** Panels (1)–(4) denote the input images, and panels (a)–(d) correspond to IMPUS, DiffMorpher, FreeMorph, and CHIMERA (Ours), respectively. The same convention applies to panels (e)–(h).





Figure 10. **Qualitative comparison showing the results of challenging 14-image morphing (compared to 5-image morphing).** Panels (1)–(4) denote the input images, and panels (a)–(d) correspond to IMPUS, DiffMorpher, FreeMorph, and CHIMERA (Ours), respectively. The same convention applies to panels (e)–(h). Please zoom in for better visualization.





Figure 11. **Qualitative comparison showing the results of challenging 14-image morphing (compared to 5-image morphing).** Panels (1)–(4) denote the input images, and panels (a)–(d) correspond to IMPUS, DiffMorpher, FreeMorph, and CHIMERA (Ours), respectively. The same convention applies to panels (e)–(h). Please zoom in for better visualization.

IDM Ablation - Fixed Inversion Timestep					
	FID <sub>local</sub> ↓	FID <sub>global</sub> ↓	LPIPS ↓	PPL ↓	GCSR ↑
(a) Ours	<b>173.248</b>	<b>89.064</b>	<b>1.666</b>	<b>0.278</b>	<b>89.592</b>
(b) Early	<u>182.749</u>	<u>92.159</u>	1.801	0.300	<u>88.218</u>
(c) Mid	188.432	94.154	1.800	0.300	87.887
(d) Late	199.500	101.102	<u>1.748</u>	<u>0.291</u>	87.599

Table 6. **Ablation of inversion-denoising timestep mapping (IDM).** We fix the inversion timesteps while performing injections at multiple denoising timesteps.

## B. Qualitative Result of ACI Injection Weight

As shown in Fig. 12 (a) (red arrow), when the injection weight in ACI is set too small, the results exhibit over-smoothing and saturated colors. This indicates that, without a sufficient ACI effect, the diffusion model tends to produce its characteristic artifacts. In addition, the 2nd, 3rd, and 4th column images in Fig. 12 (c) (red arrow) become noticeably noisy, and the 1st–4th images in Fig. 12 (d) (red arrow) generate glasses that do not exist in the input image, while the outputs also appear noisy and blurry. These observations show that when the ACI weight is overly large, the morphing trajectory is excessively constrained, causing high-frequency details that do not exist in the original images to be injected.

## C. Ablation Study on Inversion-Denoising Timestep Mapping (IDM)

In this section, we present additional experimental results on the effectiveness of the Inversion-Denoising Timestep Mapping (IDM) described in Sec. 4.1. To validate the benefit of IDM, we compare the case where the mapping function is used (Ours) with the case where it is not used, and we report both qualitative and quantitative results. We divide the non-mapping cases into two configurations: (i) the inversion timesteps are fixed to early, mid, or late regions, and the denoising process injects the corresponding fixed cached layers for each timestep; (ii) the inversion timesteps are extracted at all timesteps as in the original setting, but the denoising process injects the cached features only within one fixed region (early, mid, late). For clarity, we unify the interpretation of early, mid, and late as follows: early denotes the state with the least injected noise, mid denotes a medium noise level, and late denotes the highest noise level (although, in practice, early denoising timesteps contain high noise and late timesteps contain almost no noise).

When the inversion timesteps are fixed, Table 6 shows that our IDM-based model (a) achieves the best quantitative performance. As illustrated in Fig. 13, fixing inversion to early, mid, or late produces undesired results: the model generates images that deviate from the input images *A* and

IDM Ablation - Fixed Denoising Timestep					
	FID <sub>local</sub> ↓	FID <sub>global</sub> ↓	LPIPS ↓	PPL ↓	GCSR ↑
(a) Ours	<b>173.248</b>	<b>89.064</b>	<b>1.666</b>	<b>0.278</b>	<b>89.592</b>
(b) Early	<u>195.510</u>	<u>98.609</u>	1.858	0.310	<u>86.588</u>
(c) Mid	206.403	103.627	1.747	0.291	84.819
(d) Late	206.036	102.629	<u>1.741</u>	<u>0.290</u>	85.176

Table 7. **Quantitative evaluation with respect to the IDM.** We fix the denoising timesteps while extracting multiple inversion timesteps.

*B* (Fig. 13 (b), (c)), or produces structurally unstable results with severe artifacts (Fig. 13 (d)). In each case, the red arrows in the figure explicitly indicate the regions where these degradations occur.

When the denoising timesteps are fixed, Table 7 again shows that the IDM-based model (a) provides the best quantitative results. As shown in Fig. 14, injecting cached features only at early, mid, or late denoising timesteps leads to several issues: overly saturated images (Fig. 14 (b)) or images that are noticeably blurry or noisy (Fig. 14 (c), (d)). In these cases, the red arrows explicitly indicate the regions corresponding to the undesired artifacts and noise.

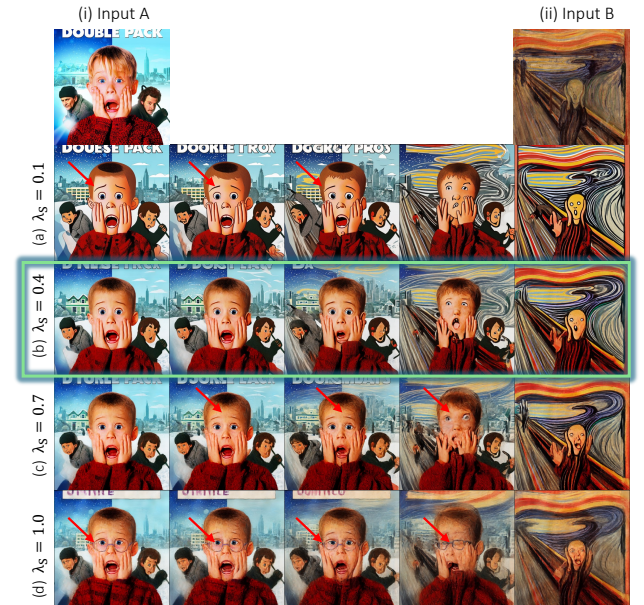


Figure 12. **Qualitative results for different injection weights of the cached ACI features in the denoising process.** (i) and (ii) denote the input image pair, and (a)–(d) show the results for  $\lambda_s$  values of 0.1, 0.4, 0.7, and 1.0, respectively.

## D. Evaluation Metric

This section provides detailed explanations of the metrics introduced in Fig. 5. The motivation, significance, and limitations of these metrics are further discussed in Sec. 4.3.



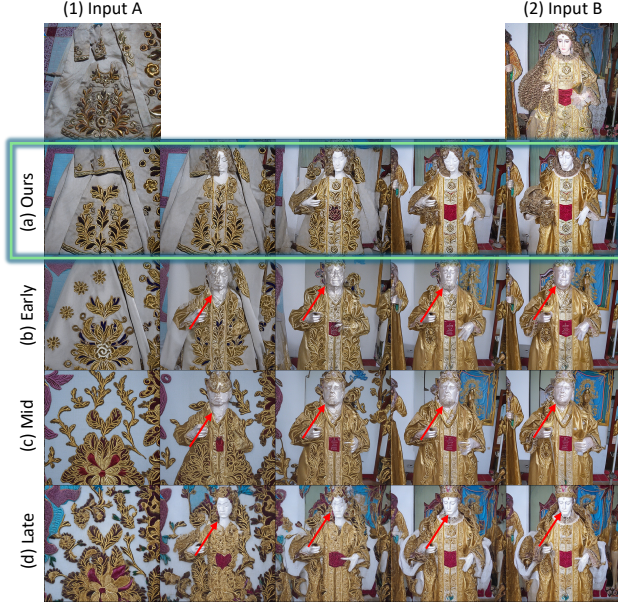


Figure 13. **Qualitative results when the inversion timesteps are fixed.** Panels (b) Early, (c) Mid, and (d) Late correspond to states with high noise, medium noise, and no noise, respectively. Panel (a) represents our model with the IDM applied.

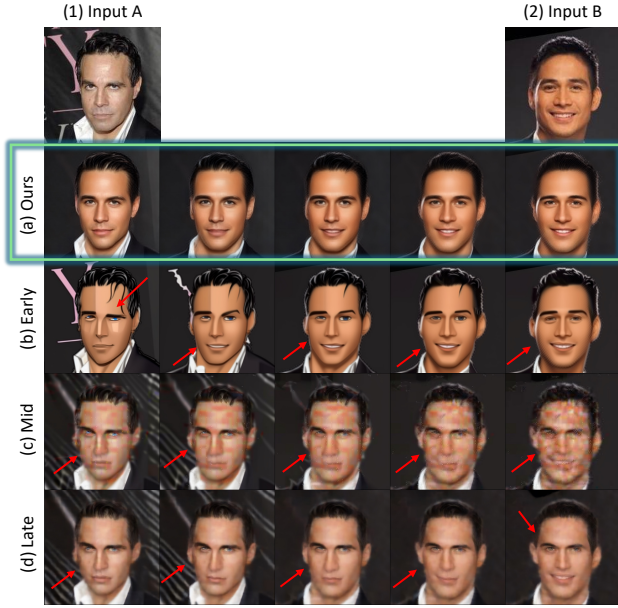


Figure 14. **Qualitative results when the denoising timesteps are fixed.** Panels (b) Early, (c) Mid, and (d) Late correspond to states with high noise, medium noise, and no noise, respectively. Panel (a) represents our model with the IDM applied.

## D.1. Fréchet Inception Distance (FID)-Based Metrics

**Local FID.** We use a local variant,  $\text{FID}_{\text{local}}$ , to measure distribution gaps between the input image pair  $\{A, B\}$  and the morphing images  $\{I_k\}_{k=1}^K$  on a per-pair basis. For an image pair  $j$ , the input images  $\{A_j, B_j\}$  serve as the real domain, and the morphing images  $\{I_k^{(j)}\}_{k=1}^{K_j}$  serve as the generated domain. Let

$$X_{\text{real}}^{(j)} = \{f(A_j), f(B_j)\}, \quad X_{\text{gen}}^{(j)} = \{f(I_k^{(j)})\}_{k=1}^{K_j}. \quad (10)$$

The local FID for pair  $j$  is defined as:

$$\text{FID}_{\text{local}}^{(j)} = \text{FID}(\{A_j, B_j\}, \{I_k^{(j)}\}_{k=1}^{K_j}), \quad (11)$$

which measures how well the morphing frames align with the endpoint distribution for each pair. At the dataset level, we compute:

$$\overline{\text{FID}}_{\text{local}} = \frac{1}{N} \sum_{j=1}^N \text{FID}_{\text{local}}^{(j)}, \quad (12)$$

to summarize pair-wise domain consistency.

**Global FID.** In contrast,  $\text{FID}_{\text{global}}$  evaluates the distribution gap at the dataset level. Let

$$\mathcal{X}_{\text{real}} = \bigcup_{j=1}^N \{A_j, B_j\}, \quad \mathcal{X}_{\text{gen}} = \bigcup_{j=1}^N \{I_k^{(j)}\}_{k=1}^{K_j}. \quad (13)$$

We estimate the mean and covariance of each set and apply the standard FID formula:

$$\text{FID}_{\text{global}} = \text{FID}\left(\bigcup_{j=1}^N \{A_j, B_j\}, \bigcup_{j=1}^N \{I_k^{(j)}\}_{k=1}^{K_j}\right), \quad (14)$$

Thus,  $\text{FID}_{\text{local}}$  measures pair-wise domain alignment, while  $\text{FID}_{\text{global}}$  captures how well the model preserves the input images distribution at the dataset level.

## D.2. Learned Perceptual Image Patch Similarity (LPIPS)-Based Metrics

**LPIPS.** For each image pair  $j$ , we define an ordered path

$$J_0^{(j)} = A_j, \quad J_k^{(j)} = I_k^{(j)} \quad (k = 1, \dots, K_j), \quad J_{K_j+1}^{(j)} = B_j. \quad (15)$$

We compute pairwise LPIPS distances using  $L(\cdot, \cdot)$ :

$$d_n^{(j)} = L(J_{n-1}^{(j)}, J_n^{(j)}), \quad n = 1, \dots, K_j + 1. \quad (16)$$



The path-based LPIPS metric is then defined as:

$$\text{LPIPS}^{(j)} = \sum_{n=1}^{K_j+1} d_n^{(j)}, \quad (17)$$

and its dataset-level average is

$$\overline{\text{LPIPS}} = \frac{1}{N} \sum_{j=1}^N \text{LPIPS}^{(j)}. \quad (18)$$

### D.3. Perceptual Path Length (PPL)

The Perceptual Path Length (PPL) [22] measures the smoothness of the generator mapping by quantifying how sensitively the generated image changes under small perturbations in the latent space. Given a generator  $g : \mathcal{W} \rightarrow \mathcal{Y}$  and two nearby latent codes  $\mathbf{w}, \mathbf{w}' \in \mathcal{W}$  sampled along a linear interpolation, the PPL is defined as the expected perceptual distance between the corresponding images, normalized by the squared step size in latent space:

$$\text{PPL} = \mathbb{E}_{\mathbf{w}, \mathbf{w}'} \left[ \frac{d_{\text{LPIPS}}(g(\mathbf{w}), g(\mathbf{w}'))}{\|\mathbf{w} - \mathbf{w}'\|_2^2} \right],$$

where  $d_{\text{LPIPS}}(\cdot, \cdot)$  denotes the LPIPS perceptual distance computed in a deep feature space. This metric approximates the local curvature of the generator manifold, and lower PPL values indicate a smoother, more semantically consistent latent-to-image mapping.

## E. Detail Description of GLCS

Let  $A$  and  $B$  be the endpoint images, and let  $\{I_k\}_{k=1}^K$  be the predicted morphing images ordered from  $A$  to  $B$ . We adopt a DiffSim-based bounded similarity [45], denoted by

$$s(X, Y) \in [-1, 1], \quad (19)$$

which is implemented as a cosine similarity in a diffusion feature space and primarily captures low-level similarity, unlike LPIPS. In practice, this makes  $s(\cdot, \cdot)$  sensitive to both style and semantic correspondence between images.

For each index  $k$ , we define the normalized interpolation weight

$$\alpha_k = \frac{k+1}{K+1}, \quad k = 0, \dots, K-1, \quad (20)$$

where  $\alpha_k$  encodes the ideal mixing ratio between the two endpoints  $A$  and  $B$ .

For convenience, we denote the similarities between each frame and the endpoints as

$$s_X(k) = s(X, I_k), \quad X \in \{A, B\}, \quad (21)$$

and introduce a clamping operator to the unit interval,

$$[x]_0^1 = \min(1, \max(0, x)), \quad (22)$$

so that all per-frame consistency terms are normalized to  $[0, 1]$ .

**(i) Global Consistency Score (GCS).** We first model the global expected trend of similarities along the morphing sequence. Given the four endpoint similarities

$$s(A, A), s(A, B), s(B, A), s(B, B), \quad (23)$$

we define the expected similarity of frame  $I_k$  to each endpoint  $X \in \{A, B\}$  using spherical interpolation (`slerp`) in similarity space:

$$\bar{s}_X(k) = \text{slerp}(s(X, A), s(X, B); \alpha_k). \quad (24)$$

Using this expected trend, we define the per-frame global consistency term as

$$g_k = [1 - |s_A(k) - \bar{s}_A(k)|]_0^1 \cdot [1 - |s_B(k) - \bar{s}_B(k)|]_0^1, \quad (25)$$

where each factor evaluates how well the measured similarity  $s_X(k)$  matches the expected similarity  $\bar{s}_X(k)$  for  $X \in \{A, B\}$ .

We optionally sharpen the sensitivity of this term by applying an exponent  $\gamma \geq 1$ ,

$$\tilde{g}_k = g_k^\gamma, \quad (26)$$

where  $\gamma > 1$  penalizes deviations from the expected trend more strongly.

Finally, we define the Global Consistency Score (GCS) as

$$\text{GCS} = \frac{1}{K} \sum_{k=0}^{K-1} \tilde{g}_k. \quad (27)$$

**(ii) Local Consistency Score (LCS).** To capture local smoothness along the morphing trajectory, we define a local expectation that relates each frame to its temporal neighbors. For each  $X \in \{A, B\}$ , we first estimate the locally expected similarity at index  $k$  as:

$$\tilde{s}_X(k) = \begin{cases} s_X(1), & k = 0, \\ \frac{1}{2}(s_X(k-1) + s_X(k+1)), & 0 < k < K-1, \\ s_X(K-2), & k = K-1, \end{cases} \quad (28)$$

where boundary images use their single temporal neighbor and interior images use the average of the preceding and succeeding images.

Using  $\tilde{s}_X(k)$ , we define the per-frame local consistency term as

$$\ell_k = [1 - |s_A(k) - \tilde{s}_A(k)|]_0^1 \cdot [1 - |s_B(k) - \tilde{s}_B(k)|]_0^1, \quad (29)$$

which measures whether the similarity to each endpoint evolves smoothly when compared to neighboring images. The resulting Local Consistency Score (LCS) is given as:

$$\text{LCS} = \frac{1}{K} \sum_{k=1}^K \ell_k. \quad (30)$$

**(iii) Global-Local Consistency Score (GLCS).** Finally, we combine these two complementary components into our morphing-oriented metric, the **Global-Local Consistency Score (GLCS)**, defined as:

$$\text{GLCS} = \sqrt{\text{GCS} \cdot \text{LCS}}. \quad (31)$$

The full algorithm for GLCS is provided in Algorithm 2.

### E.1. Effects of GCS and LCS

Fig. 15 reports the effect of GCS on selected morphing images. In Fig. 15 (a) and (b), the red lines and dots indicate cases with low GCS scores, while the blue lines and dots indicate cases with high GCS scores. In Fig. 15 (a), the Morphing-0 image is highly similar to image *A* and also shares a similar background with Morphing-1, resulting in a high GCS score of 90.789. In contrast, Morphing-1 should strongly reflect the wolf and moderately reflect the human from image *A*, but it fails to do so, leading to a low GCS score. Moreover, Morphing-2 does not properly reflect either the wolf or the human, and thus shows the lowest score among the morphing images (Fig. 15 (b) shows a similar case). Unlike (a) and (b), panels (c) and (d) exhibit consistently high GCS values across the morphing sequence, and human observers also perceive strong domain consistency that includes both domains of *A* and *B*. This indicates that (c) and (d) have higher domain consistency than (a) and (b). These results demonstrate that the proposed GCS can evaluate domain consistency in a manner that aligns well with human perception.

Fig. 16 reports the effect of LCS on selected morphing images. In Fig. 16 (a) and (b), the red arrows indicate images with low perceptual smoothness, while the blue lines indicate images with high perceptual smoothness. We observe that the LCS score decreases as the difference between adjacent frames increases. In Fig. 16 (c) and (d), we report transitions where the LCS values are consistently high across the morphing sequence. Human observers also perceive the transitions in (c) and (d) as smoother than those in (a) and (b), and our metric assigns higher scores to these transitions. These results show that the proposed LCS can evaluate perceptual smoothness in a way that is consistent with human judgment.

### E.2. Comparison between traditional metric and GLCS

Fig. 17 provides a qualitative comparison between  $\text{FID}_{\text{local}}$  and GCS. As shown in Fig. 17, the first rows of (a) and (b)

achieve better  $\text{FID}_{\text{local}}$  scores than the second rows. However, visual inspection reveals that the third image in the first row of (a) does not properly include both domains of *A* and *B*, and the fourth image even produces a result that is unrelated to image *B*. Similarly, in the first row of (b), the third and fourth images contain almost no elements from image *B*. These observations indicate that  $\text{FID}_{\text{local}}$  does not align well with human perception when evaluating domain consistency, since it only compares the overall distributions of *A*, *B* and the morphing images.

In contrast, the proposed GCS evaluates whether each image properly reflects both domains of *A* and *B* according to the interpolation ratio. As a result, the second rows of (a) and (b), which better preserve domain consistency, are assigned higher quality scores than the first rows. This demonstrates that GCS provides a more human-aligned assessment of domain consistency.

Fig. 18 presents a qualitative comparison between LPIPS, PPL, and LCS. As shown in Fig. 18, the first rows of (a) and (b) obtain higher LPIPS and PPL scores than the second rows. However, visual inspection shows that the second rows exhibit smoother transitions than the first rows. This indicates that LPIPS and PPL do not align well with human perception when evaluating smoothness, as they rely on VGG- and GAN-based networks.

In contrast, the proposed LCS leverages DiffSim [45], which measures diffusion-based similarity and benefits from diffusion priors to better match human perception. As a result, LCS assigns higher scores to the second rows in Fig. 18 (a) and (b), which are perceived as smoother by human observers. These results demonstrate that the proposed LCS provides a perceptually aligned measure of transition smoothness.

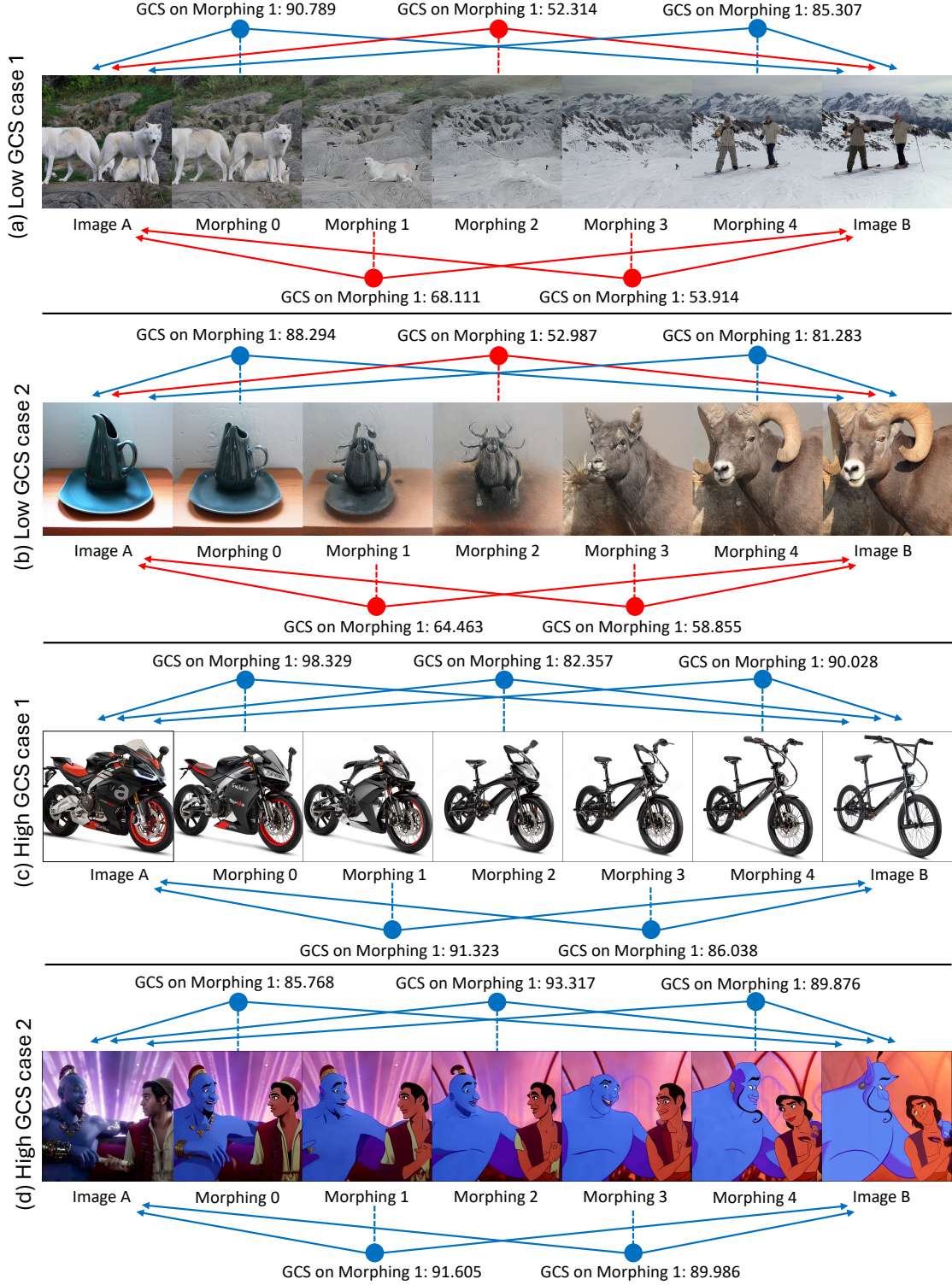


Figure 15. **Qualitative examples showing how the GCS component of GLCS aligns with human perception.** Blue arrows indicate frames where the domains of  $A$  and  $B$  are properly mixed according to the perceived interpolation ratio, while red arrows indicate frames where the two domain cues are not well reflected given the same interpolation ratio.



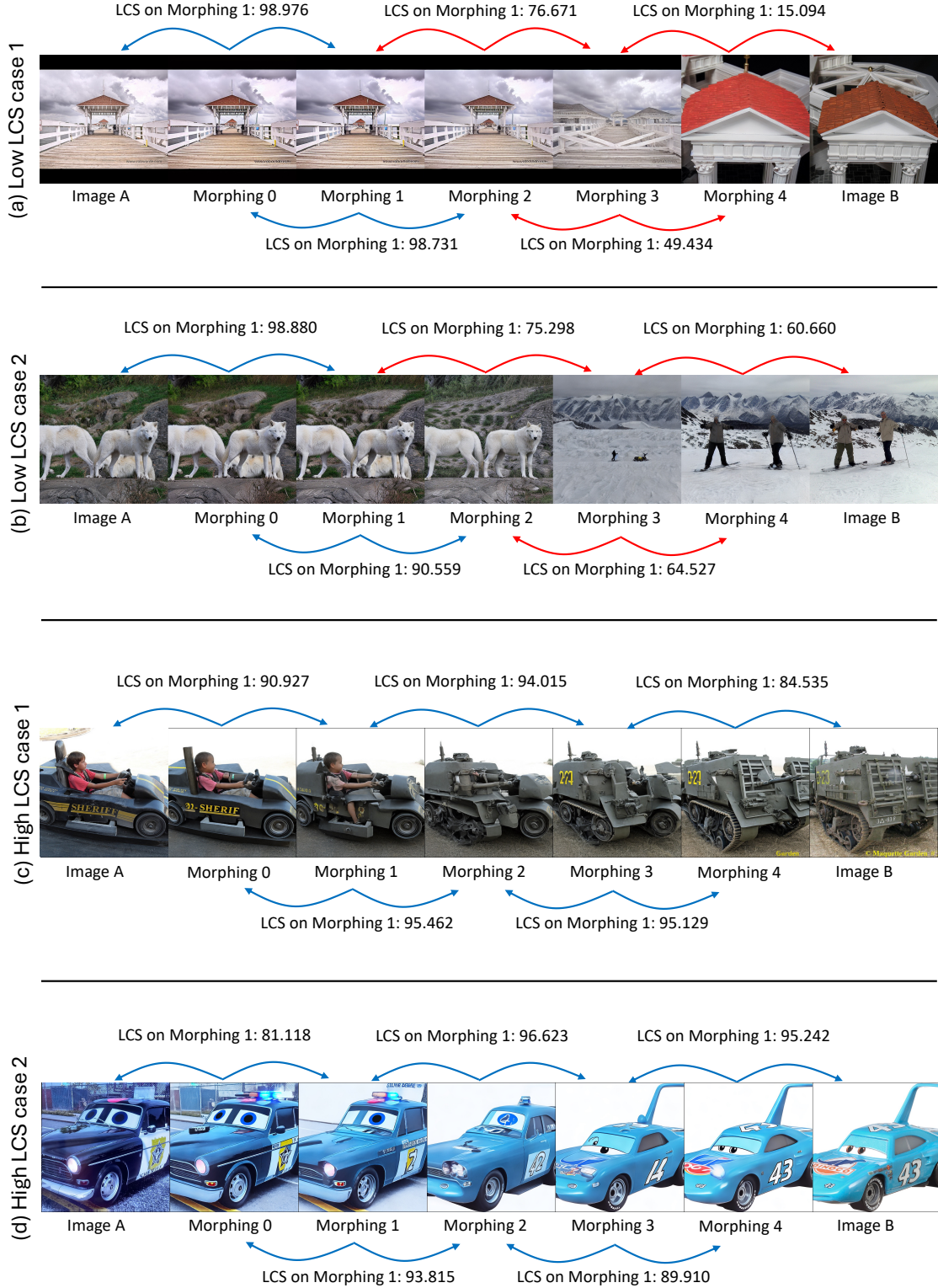


Figure 16. **Qualitative examples showing how the LCS component of GLCS aligns with human perception.** Blue arrows indicate cases that are judged as similar by human observers, while red arrows indicate cases with abrupt perceptual changes.



Figure 17. **Qualitative comparisons between  $FID_{local}$  and GCS, which is a component of our proposed metric.** Panels (a) and (b) present qualitative results for two different cases.

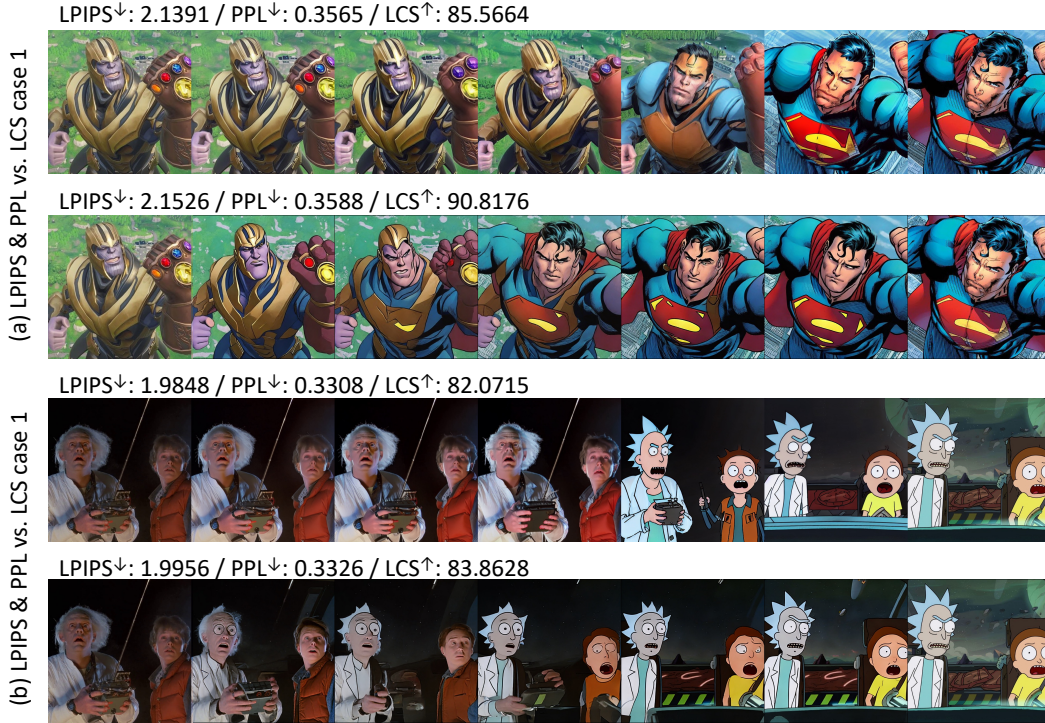


Figure 18. **Qualitative comparisons between LPIPS, PPL, and LCS, which is a component of our proposed metric.** Panels (a) and (b) present qualitative results for two different cases.



---

**Algorithm 1** CHIMERA with Adaptive Cache Injection and Semantic Anchor Prompting (Fig. 4)

---

**Input:** input image pair  $A, B$ ; number of morphing images  $K$ ; DDIM inversion steps  $N_{\text{inv}}$ ; denoising steps  $N_{\text{dng}}$ ; cached layer set  $S \in \{D, M, U\}$ ; ACI weights  $\{\lambda_S\}_S$ .

**Output:** morphing sequence  $\{I_k\}_{k=0}^{K-1}$ .

**Step 1: DDIM inversion and cache collection.**

1: For each  $X \in \{A, B\}$ , run DDIM inversion to obtain the inverted latent  $z_X$  and cached multi-scale U-Net features  $H_S(X, t)$  as in Eq. 3.

**Step 2: Morphing latent construction and cache blending.**

2: For  $k = 0, \dots, K-1$ , compute interpolation weight  $\alpha_k$  and construct the morphing latent  $z_k$  via Eq. 2  
3: For each inversion step  $t$  and each scale  $S \in \{D, M, U\}$ , construct the blended cached feature  $\hat{C}_S(k, t)$  via Eq. 4

**Step 3: Semantic Anchor Prompting (SAP) setup.**

4: Query a VLM with  $(A, B)$  to obtain text triplet  $(\text{text}_{\text{anc}}, \text{text}_A, \text{text}_B)$  and encode them to  $(e_{\text{anc}}, e_A, e_B)$  as in Sec. 4.2 (used in Eq. 8).

**Step 4: Denoising with Adaptive Cache Injection (ACI) and SAP.**

5: **for**  $k = 0, \dots, K-1$  **do**  
6: Initialize latent  $x_{\tau_0}^{(k)} \leftarrow z_k$ .  
7: **for** each denoising step  $\tau \in \mathcal{T}_{\text{dng}}$  **do**  
8: Map the denoising step to an inversion step  $t \leftarrow \phi(\tau)$  using the IDM in Eq. 5.  
9: Run the diffusion U-Net with the current latent and text embeddings to obtain  $\{F_S(\tau)\}_{S \in \{D, M, U\}}$ .  
10: For each scale  $S \in \{D, M, U\}$ , obtain the blended cached feature  $\hat{C}_S(k, \phi(\tau))$  via Eq. 6 and compute the ACI feature  $\tilde{F}_S(\tau)$  via Eq. 7.  
11: **if**  $\tau \in \mathcal{T}_{\text{SAP}}$  **then**  
12: Apply SAP by augmenting the cross-attention with the anchor-prompt as in Eq. 8 (using  $e_{\text{anc}}, e_A, e_B$ ) in the early layers.  
13: **end if**  
14: Update the latent  $x_{\tau+1}^{(k)}$  by one diffusion denoising step.  
15: **end for**  
16: Decode the final latent  $x_{\tau_{\text{final}}}^{(k)}$  with the VAE decoder to obtain  $I_k = \text{VAE}^{-1}(x_{\tau_{\text{final}}}^{(k)})$ .  
17: **end for**

18: **return** morphing sequence  $\{I_k\}_{k=0}^{K-1}$ .

---



---

**Algorithm 2** Computation of the Global-Local Consistency Score (GLCS)

---

**Input:** endpoint images  $A, B$ ; morphing images  $\{I_k\}_{k=1}^K$ ; DiffSim-based bounded similarity  $s(\cdot, \cdot) \in [-1, 1]$ ; sharpening exponent  $\gamma \geq 1$ .

**Output:** Global Consistency Score GCS, Local Consistency Score LCS, and Global-Local Consistency Score GLCS.

**Step 1: Similarity computation.**

1: **for**  $X \in \{A, B\}$  **do**  
2: **for**  $k = 1, \dots, K$  **do**  
3: Compute per-frame similarity  $s_X(k)$  according to Eq. 21.  
4: **end for**  
5: **end for**  
6: Compute endpoint similarities  $s(X, Y)$  for all  $X, Y \in \{A, B\}$  as in Eqs. 19 and 23.

**Step 2: Global Consistency Score (GCS).**

7: **for**  $k = 1, \dots, K$  **do**  
8: Compute normalized interpolation weight  $\alpha_k$  as in Eq. 20.  
9: **for**  $X \in \{A, B\}$  **do**  
10: Compute expected global similarity  $\bar{s}_X(k)$  using spherical interpolation, following Eq. 24.  
11: **end for**  
12: Compute global consistency term  $g_k$  using Eq. 25.  
13: Apply sharpening to obtain  $\tilde{g}_k$  according to Eq. 26 (with exponent  $\gamma$ ).  
14: **end for**  
15: Aggregate  $\{\tilde{g}_k\}_{k=1}^K$  to obtain the Global Consistency Score GCS using Eq. 27.

**Step 3: Local Consistency Score (LCS).**

16: **for**  $k = 1, \dots, K$  **do**  
17: **for**  $X \in \{A, B\}$  **do**  
18: Compute locally expected similarity  $\bar{s}_X(k)$  from neighboring images according to Eq. 28.  
19: **end for**  
20: Compute local consistency term  $\ell_k$  using Eq. 29.  
21: **end for**  
22: Aggregate  $\{\ell_k\}_{k=1}^K$  to obtain the Local Consistency Score LCS using Eq. 30.

**Step 4: Global-Local Consistency Score (GLCS).**

23: Combine GCS and LCS to obtain the Global-Local Consistency Score GLCS according to Eq. 31.

24: **return** GCS, LCS, GLCS.

**where**  $[x]_0^1$  denotes the clamping operator defined in Eq. 22 and used in Eqs. 25 and 29, and  $s(\cdot, \cdot)$  is the DiffSim-based similarity introduced in Eq. 19.

---

## F. Detailed Analyses of SAP

**Prompting Strategy.** To obtain stable and semantically aligned anchor-prompts for SAP, we employ a structured VLM prompting strategy. Unlike generic captioning models that independently describe each input image, our prompt explicitly instructs the VLM to extract shared semantic meaning or shared layout structure across the two endpoints. This ensures that the generated anchor-prompt captures the core concept connecting both images, which is essential for guiding semantic alignment during the denoising process.

As shown in Fig. 19, the VLM [2] outputs per-image captions ( $text_A, text_B$ ) and a shared anchor-prompt ( $text_{anc}$ ). The anchor-prompt highlights the semantic or structural component common to both images, and SAP uses this information to maintain semantic coherence across the morphing sequences. The same template is applied to all image pairs and datasets used in our experiments. The full prompt template is provided below.

### Prompt template used for Qwen2.5-VL.

You are given two correlated images.  
Your goal is to analyze them in a way that helps to generate smooth and semantically consistent transitions between the two.

1. First, carefully identify their shared semantic concept, the main subject, action, or event that connects both images.
2. Next, identify their shared layout structure, the spatial arrangement or composition of major elements (e.g., background, perspective, subject position) that remains partially consistent between both.
3. Summarize the shared theme (semantic and/or layout) in one short compact phrase.
4. Then, write short but precise captions for each image, ensuring that both captions naturally include the shared semantic meaning and layout structure.

Use this exact format strictly:

Anchor-prompt: [compact phrase capturing shared semantic or layout aspect]

Caption A: [short factual description of image1 including the shared theme]

Caption B: [short factual description of image2 including the shared theme]

Avoid artistic or stylistic adjectives (e.g., “beautiful”, “vibrant”). Focus only on semantic meaning and spatial arrangement, not texture, color tone, or artistic style.

### Output format.

Anchor-prompt: [compact shared concept]

Caption A: [description of image A including the shared theme]

Caption B: [description of image B including the shared theme]

Avoid artistic or stylistic adjectives; focus strictly on semantics and spatial structure.

Table 8 disentangles the impact of the VLM prompting strategy and our architectural components. Row (a) starts from a FreeMorph-based [7] baseline, where we replace the original shared DDIM inversion with per-endpoint DDIM

SAP ablation on Prompting Strategy					
	FID <sub>local</sub> ↓	FID <sub>global</sub> ↓	LPIPS ↓	PPL ↓	GLCS ↑
(a) Our base w/ Llava	226.122	110.595	1.892	0.315	88.132
(b) Our base w/ Qwen	205.486	100.856	1.935	0.322	87.946
(c) Our base w/ Qwen + SAP	209.331	101.971	1.906	0.317	88.053
(d) CHIMERA (Ours)	173.248	89.064	1.666	0.278	89.592

Table 8. Ablation on the VLM prompting strategy and the SAP/ACI modules.

Morphing-optimized vs. descriptive text conditions					
	FID <sub>local</sub> ↓	FID <sub>global</sub> ↓	LPIPS ↓	PPL ↓	GLCS ↑
(a) Ours	173.248	89.064	1.666	0.278	89.592
(b) Our base w/ Llava	178.873	90.128	1.631	0.272	88.600

Table 9. Ablation on text conditions with the CHIMERA backbone, SAP, and ACI fixed. (a) uses our morphing-optimized text interface (Qwen-based anchor-prompt with two correlated per-image captions), whereas (b) reverts to descriptive FreeMorph-style captions with two independently generated descriptions and no anchor-prompt.

inversion [32], while keeping the LLaVA-based [31] VLM and its original prompts. In row (b), we swap LLaVA for Qwen [2] and enforce a correlated caption design, where the two endpoint captions are generated to explicitly share common semantics but no anchor-prompt or SAP is used. This modification alone already reduces both local and global FID, suggesting that a stronger VLM and semantically tied per-image prompts improve morphing quality even without changing the diffusion backbone. Row (c) then adds our SAP module on top of the same Qwen-based prompting, additionally introducing an anchor-prompt that summarizes the semantics shared by the two endpoints. Although the gains over (b) are moderate, GLCS increases without degrading FID, indicating that SAP stabilizes semantic transitions rather than merely trading off fidelity. Finally, row (d) combines the correlated Qwen prompting, SAP, and ACI, yielding the full CHIMERA model. This configuration achieves the best scores across FID, LPIPS, PPL, and GLCS, showing that both the proposed prompting strategy and the SAP/ACI modules contribute jointly to the overall performance improvement.

**Morphing-Optimized Text Conditions vs Descriptive Text Conditions.** Most prior diffusion-based morphing pipelines [7, 24, 27] adopt generic, single-image captioning models and reuse their per-image descriptions as conditioning. In such settings, the textual interface is not explicitly tailored to the requirements of morphing, namely smooth and symmetric evolution along a path between two endpoints. In contrast, CHIMERA treats the captioning stage as an integral part of the model design: our Qwen-based VLM [2] is prompted to produce a shared anchor-prompt and two correlated per-image captions that are jointly opti-













Input A   Input B		Text Prompts	
		FreeMorph [ICCV'25]	Ours
		<p><i>text<sub>A</sub></i>: "A young puppy with a pink tongue and a happy expression in a green outdoor setting."</p> <p><i>text<sub>B</sub></i>: "A brown dog with a pink nose and tongue in a room."</p>	<p><i>text<sub>A</sub></i>: "A close-up of a golden puppy with its <b>tongue out</b>, looking cheerful"</p> <p><i>text<sub>B</sub></i>: "A fluffy brown dog with wide eyes and an <b>open mouth</b>, exuding happiness"</p> <p><i>text<sub>anc</sub></i>: "<b>Happy dogs with open mouths</b>"</p>
		<p><i>text<sub>A</sub></i>: "A man with white hair and a surprised expression in a dark room."</p> <p><i>text<sub>B</sub></i>: "A cartoon character with spiky hair and a bald head in a car."</p>	<p><i>text<sub>A</sub></i>: "Dr. Emmett Brown and Marty McFly are shocked as they examine the flux capacitor in <b>Back to the Future</b>."</p> <p><i>text<sub>B</sub></i>: "Rick and Morty express surprise during a space journey in <b>Rick and Morty</b>."</p> <p><i>text<sub>anc</sub></i>: "<b>Science fiction time travel</b>"</p>
		<p><i>text<sub>A</sub></i>: "A chessboard with a crown and pawns in the center."</p> <p><i>text<sub>B</sub></i>: "A medieval painting depicting a religious scene with a bishop, a king, and a queen."</p>	<p><i>text<sub>A</sub></i>: "A chessboard setup featuring a queen and pawns, symbolizing strategic <b>dominance</b>"</p> <p><i>text<sub>B</sub></i>: "A king receiving a crown from a bishop, signifying the ceremonial bestowment of royal <b>authority</b>"</p> <p><i>text<sub>anc</sub></i>: "<b>Monarchical Authority</b>"</p>
		<p><i>text<sub>A</sub></i>: "A man with short brown hair and blue eyes in a black suit."</p> <p><i>text<sub>B</sub></i>: "A woman with brown hair and brown eyes in a portrait."</p>	<p><i>text<sub>A</sub></i>: "Close-up of a man at an event wearing a suit jacket, part of a <b>formal</b> red carpet appearance"</p> <p><i>text<sub>B</sub></i>: "Close-up of a woman with wavy hair, dressed <b>formally</b>, against a neutral background, likely from a photoshoot"</p> <p><i>text<sub>anc</sub></i>: "<b>Celebrity portraits with formal attire</b>"</p>
		<p><i>text<sub>A</sub></i>: "A man in a suit holding a red and blue balloon."</p> <p><i>text<sub>B</sub></i>: "A brass compass with a silver needle in a white background."</p>	<p><i>text<sub>A</sub></i>: "A man in a suit holds oversized balloons shaped like numbers, symbolizing <b>precision</b> and scale"</p> <p><i>text<sub>B</sub></i>: "An antique calculating slide rule with a metallic surface and detailed markings represents traditional methods of <b>precise</b> measurement"</p> <p><i>text<sub>anc</sub></i>: "<b>Precision in Measurement</b>"</p>

Figure 19. **Examples of VLM-generated captions and anchor prompts.** Given two endpoint images, VLM produces per-image captions ( $text_A$ ,  $text_B$ ) and a shared anchor-prompt ( $text_{anc}$ ), which is used by SAP to enforce semantic alignment during the denoising process.

mized for morphing rather than mere description.

To disentangle the effect of this morphing-oriented textual interface from architectural changes, we conduct an ablation where we keep the CHIMERA backbone, SAP, and ACI modules fixed and only vary the captioning strategy. In the *descriptive* setting, we feed CHIMERA with FreeMorph-style prompts, which consist of two independently generated captions for the endpoints; the anchor input to SAP is set to null, so no explicit shared anchor is provided. In the *morphing-optimized* setting, we use our full three-text design (anchor-prompt and two correlated captions) obtained from Qwen under the structured prompting in Sec. F. As summarized in Table 9, morphing-

optimized captions consistently improve both fidelity and GLCS over purely descriptive captions under an identical diffusion backbone, highlighting that CHIMERA is optimized for morphing starting from the text interface itself, rather than only at the level of the denoising network.

**Anchor-prompt Similarity Analysis.** To verify that the anchor-prompt indeed represents concept shared by both endpoints, we compute CLIP-based cosine similarity between the anchor text  $text_{anc}$  and each per-image caption  $text_A$  and  $text_B$  over all 76 image pairs [7]. As reported in Table 10, the anchor-prompt achieves high similarity with both endpoint captions ( $\approx 0.91$ ). This symmetric alignment

Pair type	Avg. cosine similarity	#Samples
Anchor-prompt vs. $text_A$	0.9058	76
Anchor-prompt vs. $text_B$	0.9070	76

Table 10. **Average CLIP cosine similarity between the anchor-prompt and the per-image captions on Morph4Data.** The anchor-prompt remains highly and symmetrically aligned with both endpoint captions, indicating that it captures the semantic content shared by  $text_A$  and  $text_B$  rather than collapsing toward one side.

Effect of biased anchor-prompts					
Method	FID <sub>local</sub> ↓	FID <sub>global</sub> ↓	LPIPS ↓	PPL ↓	GLCS ↑
(a) <b>Ours</b>	<b>173.248</b>	<b>89.064</b>	1.666	0.278	<b>89.592</b>
(b) Anchor=A	<u>175.033</u>	<b>89.039</b>	<b>1.657</b>	<b>0.276</b>	88.635
(c) Anchor=B	176.035	89.535	<u>1.660</u>	<u>0.277</u>	<u>88.693</u>

Table 11. **Quantitative comparison of CHIMERA with shared and biased anchor-prompts.**

suggests that the VLM [2], guided by our prompting strategy, extracts a semantic concept that is jointly supported by both endpoints, providing a stable textual anchor for SAP rather than favoring a single image.

**Effect of Biased Anchor-prompts.** To further examine the role of the anchor-prompt, we perform a controlled study in which the anchor text is forcibly modified. Concretely, we evaluate three variants: (i) *Anchor=A*, where  $text_{anc}$  is replaced by  $text_A$ ; (ii) *Anchor=B*, where  $text_{anc}$  is replaced by  $text_B$ ; and (iii) *Anchor=Irrelevant*, where  $text_{anc}$  is set to a prompt semantically unrelated to the inputs, while keeping all other components of the pipeline unchanged.

As shown in Table 11, while the biased anchors ((b) and (c)) yield comparable absolute scores, they consistently result in higher FID<sub>local</sub> and lower GLCS than the shared anchor-prompt used in CHIMERA. Qualitatively, Fig. 20 illustrates distinct failure modes for each variant. When *Anchor=A*, the transition is heavily skewed toward the source, with attributes specific to Input A (e.g., tousled hair) persisting unnaturally into later images. In contrast, when *Anchor=B*, target-specific attributes (e.g., black armor and a red-glowing eye) appear too early, causing the facial skin to take on a plastic, armor-like appearance prematurely. Most critically, the *Anchor=Irrelevant* case results in catastrophic degradation; as indicated by the red arrows in Fig. 20 (d), the absence of semantic relevance leads to severe artifacts and semantic collapse. This confirms that the anchor-prompt serves as a valid semantic bridge.

Taken together with Table 10, these observations indicate that the anchor-prompt effectively captures semantics and layout *jointly* supported by both endpoints. By enforcing

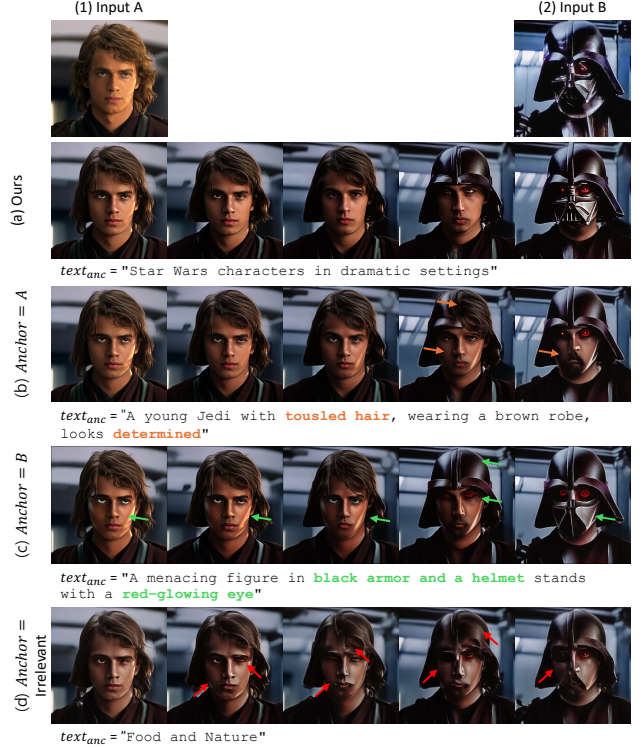


Figure 20. **Effect of biased anchor-prompts.** Qualitative comparison between our shared anchor-prompt and variants where the anchor is forced to match Input A, Input B, or an irrelevant concept. Biased anchors distort the transition, whereas the shared anchor yields the most coherent morph.

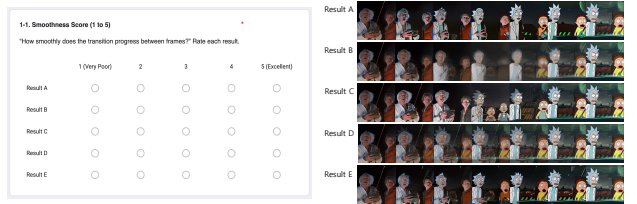


Figure 21. **User study interface and questionnaire form.**

this shared formulation through the VLM prompting strategy, SAP receives a balanced textual anchor that maintains semantic symmetry over the sequence, directly contributing to the GLCS and fidelity gains reported in Table 8.

## G. User Study: Subjective Preference Analysis

**Protocol.** We conduct a user study on 15 morphing sequences to assess how well each method aligns with human perception. For each sequence, 32 participants are shown five anonymized results (A–E) generated by CHIMERA, FreeMorph [7], DiffMorpher [27], IMPUS [24], and latent slerp (see Fig. 21). The mapping between  $\{A, \dots, E\}$  and the underlying methods is randomized per sequence and

Criteria	Method	MOS $\uparrow$	Mean rank $\downarrow$	Borda score $\uparrow$
Smoothness	<b>CHIMERA (Ours)</b>	<b>3.802</b> $\pm$ 0.468	<b>1.516</b>	<b>4.484</b>
	FreeMorph [ICCV'25]	3.025 $\pm$ 0.477	3.281	2.719
	DiffMorpher [CVPR'24]	<u>3.585</u> $\pm$ 0.482	<u>2.016</u>	<u>3.984</u>
	IMPUS [ICLR'24]	2.881 $\pm$ 0.502	3.766	2.234
	slerp	2.281 $\pm$ 0.977	4.422	1.578
Domain Consistency	<b>CHIMERA (Ours)</b>	<b>3.654</b> $\pm$ 0.499	<b>1.922</b>	<b>4.078</b>
	FreeMorph [ICCV'25]	2.735 $\pm$ 0.637	3.781	2.219
	DiffMorpher [CVPR'24]	<u>3.533</u> $\pm$ 0.509	<u>2.188</u>	<u>3.813</u>
	IMPUS [ICLR'24]	3.225 $\pm$ 0.558	2.734	3.266
	slerp	2.375 $\pm$ 0.904	4.375	1.625
Perceptual Quality	<b>CHIMERA (Ours)</b>	<b>3.600</b> $\pm$ 0.580	<b>1.859</b>	<b>4.141</b>
	FreeMorph [ICCV'25]	2.958 $\pm$ 0.600	3.203	2.797
	DiffMorpher [CVPR'24]	<u>3.419</u> $\pm$ 0.461	<u>2.391</u>	<u>3.609</u>
	IMPUS [ICLR'24]	3.290 $\pm$ 0.477	2.703	3.297
	slerp	1.894 $\pm$ 0.850	4.844	1.156
Overall Quality	<b>CHIMERA (Ours)</b>	<b>3.613</b> $\pm$ 0.586	<b>1.672</b>	<b>4.328</b>
	FreeMorph [ICCV'25]	2.917 $\pm$ 0.529	3.453	2.547
	DiffMorpher [CVPR'24]	<u>3.431</u> $\pm$ 0.435	<u>2.188</u>	<u>3.813</u>
	IMPUS [ICLR'24]	3.106 $\pm$ 0.500	2.938	3.063
	slerp	1.960 $\pm$ 0.855	4.750	1.250

Table 12. **Mean opinion scores (MOS), mean rank, and Borda score of each method in user study.** CHIMERA consistently achieves the highest MOS and best (lowest) mean rank, indicating a strong overall user preference over existing morphing methods.

Criteria	Friedman $\chi^2$	$p$ -value
Smoothness	76.190	$1.116 \times 10^{-15}$
Domain Consistency	56.866	$1.320 \times 10^{-11}$
Perceptual Quality	66.994	$9.779 \times 10^{-14}$
Overall Quality	73.480	$4.176 \times 10^{-15}$

Table 13. **Friedman test over the five methods for each subjective criterion.** In all cases, the null hypothesis that all methods are equivalent is rejected ( $p \ll 0.05$ ), confirming statistically significant differences in user ratings.

participant. Participants rate each result on a 5-point Likert scale (1–5) for four criteria: *Smoothness*, *Domain Consistency*, *Perceptual Quality*, and *Overall Quality*.

**Mean Opinion Scores.** From the resulting user–sequence–method score matrix, we first aggregate scores per participant and method and compute the mean opinion score (MOS), standard deviation, and average rank (lower is better) for each method and criterion. These statistics are summarized in Table 12. CHIMERA achieves the highest MOS and the lowest mean rank across all four criteria. DiffMorpher and IMPUS obtain MOS values close to CHIMERA for Smoothness, but their MOS and mean ranks for Domain Consistency, Perceptual Quality, and Overall Quality remain lower than those of CHIMERA. FreeMorph and slerp consistently receive lower MOS and higher (worse) mean ranks.

**Significance Test.** To test whether the observed differences are statistically meaningful, we apply a Friedman test over the five methods for each criterion, treating each partic-

Criteria	Baseline	W / T / L vs. <b>CHIMERA (Ours)</b>
Smoothness	FreeMorph [ICCV'25]	<b>32</b> / 0 / 0
	DiffMorpher [CVPR'24]	<b>18</b> / 2 / 12
	IMPUS [ICLR'24]	<b>30</b> / 1 / 1
	slerp	<b>30</b> / 0 / 2
Domain Consistency	FreeMorph [ICCV'25]	<b>32</b> / 0 / 0
	DiffMorpher [CVPR'24]	<b>15</b> / 2 / 15
	IMPUS [ICLR'24]	<b>22</b> / 1 / 9
	slerp	<b>28</b> / 0 / 4
Perceptual Quality	FreeMorph [ICCV'25]	<b>27</b> / 0 / 5
	DiffMorpher [CVPR'24]	<b>20</b> / 0 / 12
	IMPUS [ICLR'24]	<b>22</b> / 1 / 9
	slerp	<b>31</b> / 0 / 1
Overall Quality	FreeMorph [ICCV'25]	<b>31</b> / 0 / 1
	DiffMorpher [CVPR'24]	<b>18</b> / 2 / 12
	IMPUS [ICLR'24]	<b>25</b> / 1 / 6
	slerp	<b>31</b> / 0 / 1

Table 14. **Win–tie–loss statistics of CHIMERA against each baseline.** For each user and sequence, we compare the scores of CHIMERA and a baseline for a given criterion and count wins (CHIMERA > baseline), ties, and losses. CHIMERA wins in the majority of cases, showing consistent subjective superiority.

ipant as a block. Table 13 reports the resulting test statistics and  $p$ -values. For all criteria, the null hypothesis that all methods are equivalent is rejected with  $p \ll 0.05$ , indicating that the gaps observed in MOS and ranks are statistically significant.

**Pairwise Preferences.** We further analyze pairwise preferences between CHIMERA and each baseline. For every participant–sequence pair, the scores of CHIMERA and a baseline are compared for a given criterion and wins (CHIMERA > baseline), ties, and losses are counted. The win–tie–loss statistics in Table 14 show that CHIMERA wins in the vast majority of comparisons across all four criteria, while losses are rare. In particular, CHIMERA wins over FreeMorph and slerp in almost all cases, and records strictly more wins than losses against DiffMorpher and IMPUS, as also reflected in the qualitative win–tie–loss plot in Fig. 22.

**Relation to GLCS.** We further compare the user study outcomes with our GLCS-based quantitative evaluation. Among the four methods for which GLCS is defined (CHIMERA, FreeMorph, DiffMorpher, and IMPUS), CHIMERA attains the highest GLCS on both MorphBench and Morph4Data and, at the same time, achieves the highest Overall Quality MOS and the best mean rank in Table 12. Methods with lower GLCS values also tend to receive lower MOS and worse ranks in the user study, indicating that GLCS is aligned with human preference at the method level. Given this agreement between human judgments and dataset–level scores, we regard GLCS as a promising reference metric for future image morphing research, providing



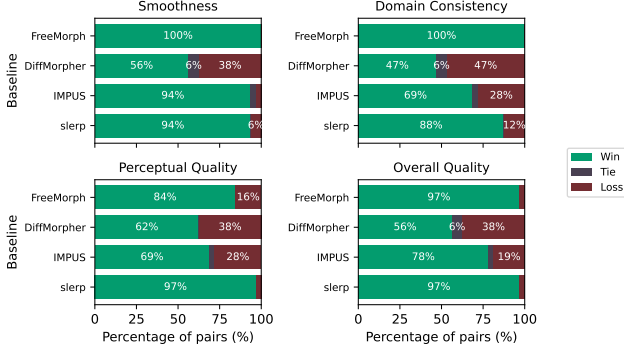


Figure 22. User study win-tie-loss ratios of CHIMERA against each baseline

Method	step1 <sub>inv</sub> [s]	step2 <sub>denoise</sub> [s]	Total [s]	Params (B)
IMPUS	32.92	18.44	478.91	1.93
DiffMorpher	3.57	60.13	64.92	1.30
FreeMorph	20.42	8.79	30.66	1.29
<b>CHIMERA (Ours)</b>	4.90	9.59	14.49	1.29

Table 15. Computation time and total number of parameters for each method.

a principled quantitative measure that jointly reflects temporal smoothness and semantic consistency.

## H. Computational Cost Report

Table 15 reports the runtime and number of parameters for the proposed CHIMERA and other methods.  $\text{step1}_{\text{inv}}$  and  $\text{step2}_{\text{denoise}}$  denote the runtime of the DDIM inversion process and the denoising process, respectively. Total indicates the overall runtime, and Params denotes the number of parameters. As shown in Table 15, the proposed CHIMERA requires fewer parameters and lower runtime than fine-tuning-based methods such as IMPUS and DiffMorpher. Moreover, CHIMERA achieves much faster runtime than the zero-shot-based method FreeMorph.

## I. Application

**Video Frame Interpolation.** Although CHIMERA is designed for still-image morphing, its capability to generate temporally dense sequences naturally suggests an application to video frame interpolation (VFI). To probe this connection, frames from VFI benchmark datasets [35, 53] are used as input, where two frames separated by a fixed temporal offset are treated as endpoints and the intermediate outputs of CHIMERA are interpreted as interpolated results. As shown in Fig. 23 on Vimeo90K-septuplet [53] some frames visually resemble reasonable interpolation, but noticeable artifacts remain. In the CHIMERA row (d), the red arrows highlight typical failure modes such as missing body parts (e.g., two arms collapsing into one) or misplaced parts

(e.g., the boy appearing with two heads). Similar issues are also observed in the other morphing baselines: IMPUS [24] (row (a)) produces implausible hand shapes or causes objects to disappear mid sequence, DiffMorpher [27] (row (b)) yields over-smoothed and blurry frames consistent with its morphing behavior, and FreeMorph [7] (row (c)) hallucinates content absent from both inputs (e.g., transforming a statue into a realistic human). On DAVIS dataset [35] in Fig. 24, where human motion and occlusions are more complex, all morphing methods exhibit pronounced non-physical deformations. CHIMERA (row (d)) generates unrealistic human bodies with truncated or severely warped arms and legs and hallucinates additional objects that do not exist in either inputs. IMPUS (row (a)) produces broken silhouettes with missing arms, DiffMorpher (row (b)) shows similar limb truncation together with strong motion blur that obscures fine details, and FreeMorph (row (c)) suffers from distorted body shapes and over-saturated colors and, like CHIMERA, sometimes hallucinates entirely new objects in the background. Overall, these observations indicate that such failures are not specific to our method but are inherent to morphing methods when applied to VFI data.

We conjecture that this stems from a fundamental mismatch between the objectives of morphing and VFI. Unlike VFI methods that establish explicit correspondences between input frames and reconstruct the motion trajectory connecting them through optical flow [33], deformable kernels [12], or learned spatiotemporal representations [25, 58], morphing models operate as generative processes that synthesize plausible in between states without being constrained to follow the true motion path. CHIMERA has no motion specific modules and receives no supervision from real videos; it is optimized for smooth transitions between two inputs rather than faithful reconstruction of motion trajectories. Moreover, CHIMERA is applied to VFI datasets in a purely zero-shot setting without domain specific fine-tuning, further widening the gap relative to VFI models. As a result, intermediate frames can traverse “imagined” states in latent space that do not correspond to physically realizable frames, which is acceptable or even desirable in morphing contexts but manifests as artifacts in VFI benchmarks.

Overall, these observations indicate that CHIMERA is distinct from reconstruction-driven VFI methods. They also suggest a natural extension: augmenting the cache and prompt-based design with explicit motion priors [29, 42, 48] and video-driven objectives [10, 51] could evolve the framework toward a VFI model that better satisfies the physical and temporal requirements of standard benchmarks.

**Creative Content Creation and Animation.** CHIMERA directly supports applications in film, game, and animation production, where artists often require smooth transi-





Figure 23. **Qualitative VFI results on Vimeo90K-septuplet.** Panels (a)–(d) correspond to IMPUS, DiffMorpher, FreeMorph, and CHIMERA (Ours), respectively. For each sequence, red arrows mark representative artifacts such as unrealistic limb configurations or duplicated local structures in the interpolated frames.

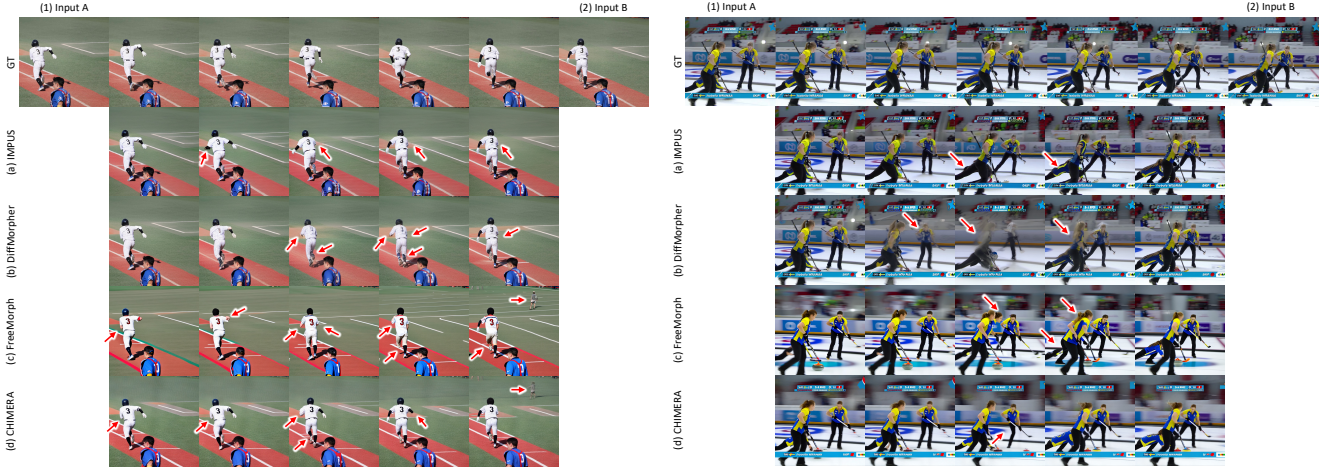


Figure 24. **Qualitative VFI results on DAVIS.** Panels (a)–(d) correspond to IMPUS, DiffMorpher, FreeMorph, and CHIMERA (Ours), respectively. The red arrows highlight severe failure cases where the interpolated results exhibit non-physical human bodies, including truncated or distorted arms and legs.

tions between disparate visual concepts. Given two images that serve as keyframes, the framework generates a temporally dense sequence of structurally consistent and semantically coherent intermediate frames without manual correspondence annotation or model fine-tuning. This capability aligns with the growing demand for engaging transitions in short-form video platforms (e.g., TikTok, Kuaishou), where visually distinctive morphing effects contribute to viewer engagement and content memorability. By providing zero-shot, training-free generation of high-quality metamorphic transitions, CHIMERA lowers the barrier for both professional creators and non-experts to prototype and deploy production-ready visual effects, ranging from character evolution and object transformations to stylized scene changes

tailored for short-form content.

## J. Limitations and Failure Cases

**Text Rendering and Typography.** While CHIMERA demonstrates superior performance in preserving semantic structure and visual realism, it shares a common limitation with other diffusion-based morphing methods [7, 24, 27] when handling images with prominent textual elements, such as logos, signage, or dense typography (see Fig. 25). In such scenarios, the generated transitions often exhibit temporally inconsistent or partially illegible glyphs, despite the surrounding spatial layout remaining coherent.

Crucially, this issue stems not from the morphing mech-



Figure 25. **Failure cases on images with prominent text.** When the endpoint images contain different words or textual layouts, all compared methods, including CHIMERA, often produce broken or unreadable characters and occasional abrupt changes in the rendered text.

anism itself, but from the inherent inductive biases of the underlying pre-trained diffusion backbones [9, 39]. Standard text-to-image models are known to treat text as high-frequency texture rather than semantic symbols, often lacking the fine-grained control required for precise glyph generation [15, 54, 59]. Consequently, since CHIMERA operates within this pretrained latent space, it inevitably inherits these typographic weaknesses, a trait observed across all competing baselines.

**Future Direction: Glyph-Aware Morphing.** We identify this limitation as a pivotal opportunity for future research. Addressing textual inconsistency necessitates moving beyond standard attention injection to incorporate explicit text-control mechanisms used in recent text manipulation research, such as layout-guided generation [59] or OCR-consistency losses [9]. We envision a *glyph-aware morphing* framework that disentangles textual content from visual style, enabling smooth interpolation of character geometries while maintaining legibility. Extending our attention composition approach to specifically target and preserve glyph structures remains a promising direction to bridge the gap between semantic morphing and precise typographic control.

## K. Additional Qualitative Result

In this section, we present additional qualitative comparisons for the 5-frame and 14-frame morphing scenarios.



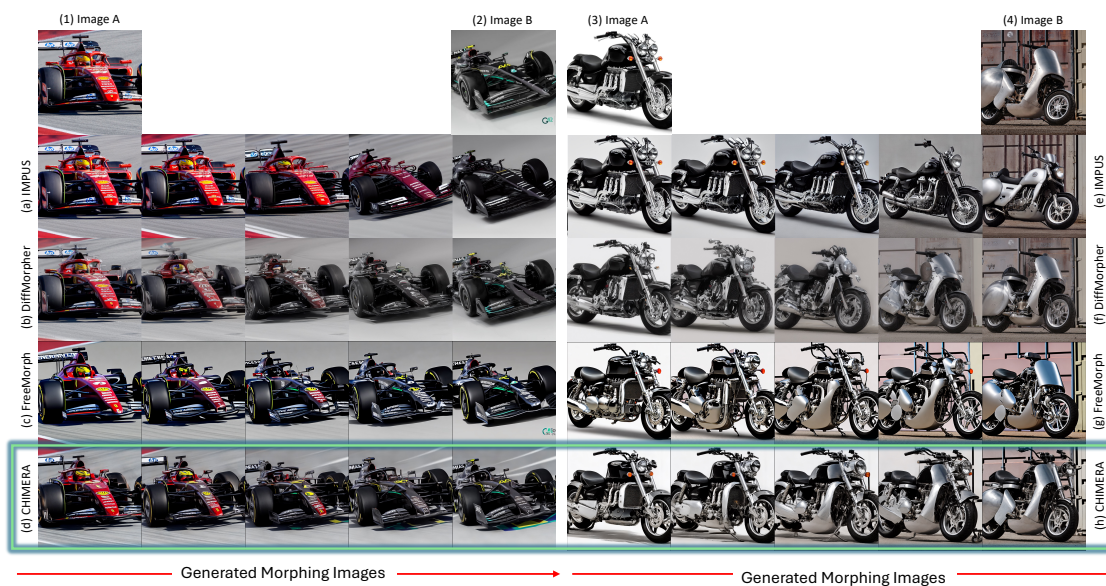


Figure 26. Additional qualitative results for 5-frame morphing.

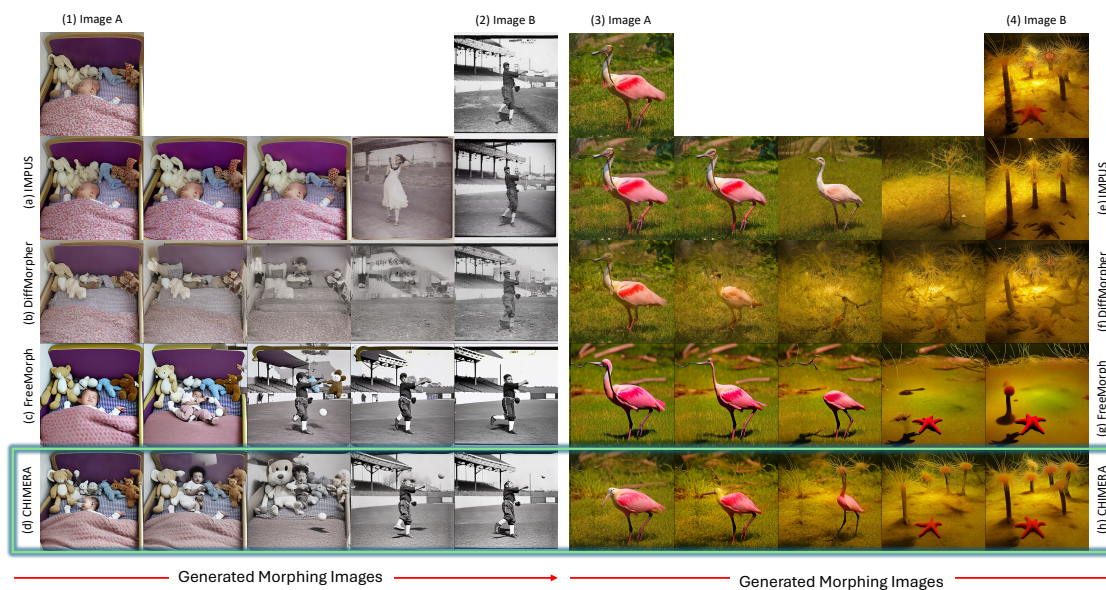


Figure 27. Additional qualitative results for 5-frame morphing.





Figure 28. Additional qualitative results for 14-frame morphing.



Figure 29. Additional qualitative results for 14-frame morphing.